



UNIVERSITY OF GREIFSWALD

MASTER THESIS

**Plasma-wall interaction in
Fluorocarbon plasmas**

Author:
Morten NAGEL

Referees:
Prof. Dr. Ralf SCHNEIDER
Prof. Dr. Jürgen MEICHSNER

Greifswald, August 15, 2012

CONTENTS

1	Motivation	1
2	Carbon fluorine plasmas and films	3
2.1	Carbon Fluorine Plasmas	3
2.2	Properties of amorphous fluorine carbon films	5
2.3	Surface reactions	6
2.4	Intermolecular forces	7
3	Introduction to Molecular Dynamics	9
3.1	Interaction potentials	10
3.2	Tersoff Potential	11
3.3	Reactive Empirical Bond-Order Potential	14
3.4	AIREBO-Potential	18
4	Numerical Implementation	21
4.1	Velocity-Verlet Algorithm	23
4.2	Estimation of the time step	24
4.3	Thermostat & Barostat	25
4.4	Allocation and removal of molecules	26
5	Results	29
5.1	Validation of the implemented changes	29
5.2	Numerical heating and switch modifications	31
5.3	Generation of surfaces	33
5.4	Results of sticking calculations	40
5.5	Sensitivity of the global model	48
6	Conclusions & Outlook	51
A	Bibliography	53
B	Appendix	59



1

MOTIVATION

Fluorocarbon plasmas are used for reactive etching in industry to build computer chips. Deposited amorphous fluorine carbon films and polymers have quite favourable properties. These are their relative high thermal stability of up to 530 K[1]. Secondly, they have an ultra low surface tension due to weak polarizability of the contained fluorine atoms. These effects are commonly used in products like GORE-TEX[2]. Thirdly, fluorocarbon films have also a low permittivity, therefore they are called a *low-k-material*. These are getting more and more interesting for the computer chip manufacturing industry as a way to reduce parasitic capacitances in smaller structures. Fourthly, fluorocarbon films have due to their *weak London dispersion force* a very low coefficient of friction [3]. As fluorocarbons are a major persistent green house gas their optimized usage should be achieved[4].

Up to now, development and research follow a trial-and-error strategy, because experimental characterization and existing models are both rather incomplete. Plasma parameters are only partly known, e.g. the density of radicals is measured but not their energy distribution. In modeling, there is a lack of integrated models of such plasmas, including plasma-wall interaction processes. Such incomplete models miss any predictive capability, because they do not resolve the fundamental non-linear characteristics of such systems. Plasma fluxes onto the walls determine both film properties and erosion or deposition dynamics through their angular, energetic and species distributions. The wall responses in terms of back-scattering, sticking or sputtering provide sinks and sources for the plasma dominating the flux balances. The existence of a wall in front of a plasma creates characteristic non-linear boundary effects on the plasma flows, producing a boundary potential reflecting most of the electrons and accelerating ions.

Even in a simplified, 0D integrated model developed by Gunnar Bandelow, similar to [5], the influence of plasma wall processes in terms of sticking coefficients on the results is quite strong as a sensitivity study shows. Additional sinks act through the non-zero sticking coefficients, therefore the system get a new equilibrium with densities different from

a pure bulk situation. Usually, sticking coefficients are not well-known and only estimates exist. Results are shown in Figure 1.1 where a reference case in red is plotted with varied sticking (other colors). By this the reference sticking coefficients of CF_3 ($\beta_{\text{CF}_3} = 0.1$), CF_2 ($\beta_{\text{CF}_2} = 0.15$) and CF ($\beta_{\text{CF}} = 0.2$) are varied with a scaling factor. The coefficients of F and C are kept constant with $\beta = 0.25$. This means that the loss channels are amplified for the three varied species. All observed species in the global model show changes in their density but in Figure 1.1 only three examples are shown. The density of the feed-gas CF_4 seems relative unaffected by the scaling factor for the sticking coefficients. But because it is the species with the largest density in the system changes of about a percent will cause big changes to other species. Interestingly with higher sticking coefficients the density for CF_4 increases slightly. The same trend appears more pronounced for F_2 which density is more than doubled in this variation study. The effect of higher sticking coefficients is contrary on the density of C_2F_4 , which is strongly reduced. More details on this sensitivity study are discussed in detail in section 5.5 using the sticking coefficients obtained in this work.

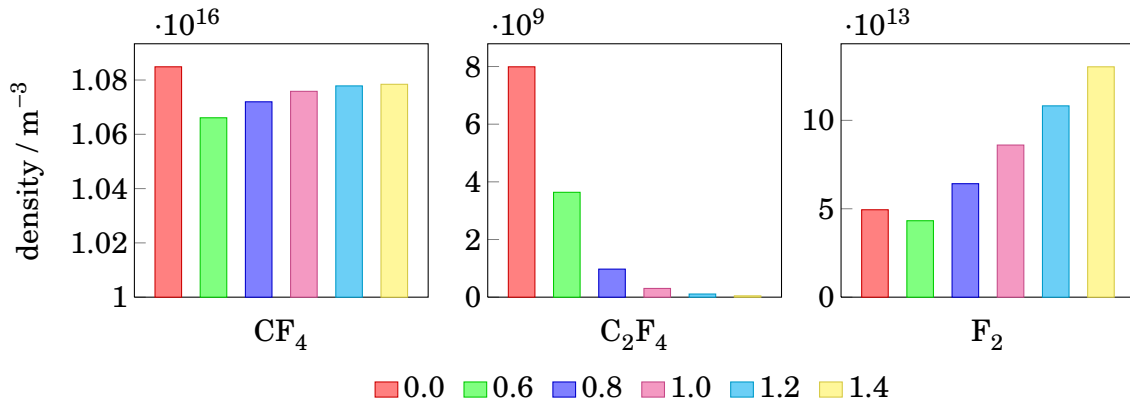


Figure 1.1: Influence of sticking on the density of selected species in the global model. The numbers in the legend are the scaling factors for an assumed stick of $\beta_{\text{CF}_3} = 0.1$, $\beta_{\text{CF}_2} = 0.15$ and $\beta_{\text{CF}} = 0.2$. The sticking coefficients $\beta_{\text{F}} = 0.25$ and $\beta_{\text{C}} = 0.25$ are constant.

The main topic of this work is the computational investigation of plasma wall interaction in *carbon fluorine plasmas*. This is done by using the method of *Molecular Dynamics*. Specifically, sticking coefficients of molecules will be calculated and their influence on the global characteristics of such plasmas will be discussed.

The structure of the thesis is as follows. At first the basic properties of carbon fluorine plasmas and films are given. Afterwards, an introduction to the computational method of Molecular Dynamics is presented, followed by a detailed discussion of the interaction potentials used, which include all information about the system and determine its properties. The specific code used in this work, LAMMPS, and own modifications and extensions in the numerical implementation are introduced. The validation strategy is discussed and results are presented on the creation of samples and sticking coefficients. The influence on these coefficients on the global, intergrated model results will be shown. At last the work is summarized and as an outlook possible extensions are given.



2

CARBON FLUORINE PLASMAS AND FILMS

In the following the basic properties of fluorine carbon plasmas and their films will be briefly presented based on Gabriel[6] and Stepanov[7], where further details can be found.

2.1 Carbon Fluorine Plasmas

Plasma is here referred to as a gas in which at least a part of ingredients is ionized. This is commonly achieved via an energy input. A standard experiment for studies of carbon fluorine plasmas and films consists of a low-pressure reactor (1 – 100 Pa) filled with stable carbon-fluorine molecules like CF_4 , C_2F_6 , C_3F_8 or C_4F_8 . In case of CF_4 a global model already exists as discussed already in 1. One of the two parallel electrodes is powered with 10 W to 200 W at a radio frequency of 13.56 MHz and the other one is grounded like the whole reactor wall (see Figure 2.1 and [8]). In this frequency range electrons experience the modulated field and respond following its time dependence due their small mass. They gain energy and atoms are ionized. This leads to the formation of the *plasma discharge*. Ions are much heavier and experience only the phase averaged electric field moving much slower than electrons.

2.2. PROPERTIES OF AMORPHOUS FLUORINE CARBON FILMS

production of HF when H₂ is added. However, a quantitative description of processes like the generation of C₂F₄ in the plasma-off phase could not be achieved yet. One possible explanation is missing surface reactions within the model[8].

Caused by the high electron mobility due to their small mass these plasma facing surfaces are charged negatively. In the plasma close to the surface a positive space charge is formed due to the strongly reduced mobility of the heavy positive ions compared to the electrons. This space charge produces a potential drop, the so-called *plasma sheath*, in which the positive ions will be accelerated. They will hit the surfaces with much higher velocity as their thermal velocity. In contrast to that, the majority of negative ions are reflected from the potential wall like the electrons and will not reach the surface. Thus, it is not necessary to investigate surface reactions of negative ions.

Plasma confinement is limited to the region between the electrodes. At the electrodes high fluxes of positive ions with high impact energies will interact with the surfaces. Outside this discharge region neutral gas without plasma is dominating. At the reactor wall much lower fluxes of neutrals with less impact energy compared to the electrodes will determine the surface reactions.

Depending on their kinetic energy at the wall incoming ions can sputter surface atoms, can stuck to the surface, can reflect from the surface or experience surface reactions. The first case is used for *plasma etching* to custom-tailor a desired structure like a deep well on a substrate. The second case is used for *plasma polymerization* where a surface is produced with polymers formed from species contained in the plasma. Even if one process dominates the others are usually still present. Also the conditions will vary in an experimental reactor. Etching may appear on the electrodes while polymers are formed at the reactor walls.

In the following the surfaces in such discharges will be characterized.

2.2 Properties of amorphous fluorine carbon films

Surfaces produced in fluorine carbon plasma are generally amorphous films with different properties, which will be discussed in this section. The key parameter for their properties is the fraction of fluorine to carbon $\kappa = \frac{N_F}{N_C}$ with N being the number density. The two extreme cases at which stable surfaces still exists are pure amorphous carbon ($\kappa = 0$) and Polytetrafluoroethylene/PTFE ($\kappa = 2$). For larger κ a stronger network of carbon atoms is built by increased cross linking with formations of carbon double bonds. This results in a harder surface. Softer fluorine carbon polymers have a higher fluorine content and consist of polymer fibers twisted into each other. The fibers stick together by *intermolecular forces* discussed in section 2.4.

The reactivity of a surface is determined by the number of dangling bonds and the amount of cross-linking. Dangling bonds are surface atoms with unsaturated open bonds. A surface with a large amount of cross-linking will be less flexible and will therefore absorb a smaller amount of energy per incoming particle compared with a surface of less cross-linking. This internal structure will be affected strongly by the production process of the film. In case of sputtering the shrinking film will contain remnants of the structures from the original material like graphite. Films grown by deposition will show less of such remnants. Surface roughness will influence the surface properties as well (see 5.4.1).

Experimental results show that κ of the surface is mainly determined by the mean energy of the impinging ions and the fraction κ in the plasma [9] or hot wire reactor[10]. A larger impact energy produces a surface with less fluorine content. Other parameters like the flux of ions and neutrals are likely to have an impact on the characteristics of the films. A large enough particle flux density prevents a complete equilibration of the surface between two particle impacts. The non-equilibrium situation provides additional energy, e.g. to break bonds. This condition is fulfilled if the time difference between subsequent particles is smaller than the equilibration-time. The equilibration is determined by the coupling to phonons resulting in 1ps[11]. This requires fluxes larger than $1 \times 10^{24} \text{ cm}^{-2} \text{ s}^{-1}$. Compared with the experimental fluxes[12] $\approx 1 \times 10^{15} \text{ cm}^{-2} \text{ s}^{-1}$ the system is far off from these conditions. Therefore, subsequent impacts can be treated independently from each other.

Experimental results for films can be summarized as follows. The cross-linking is higher with increased amount of sp^2 carbon in the surface[13–15]. The cross-linking gets larger with higher thermal stability[16]. The surface hardness decreases with growing κ [17]. The surface temperature influences the carbon hybridization as a higher temperature results in a higher sp^2 fraction[18]. Surface roughness measured in an area of $4 \mu\text{m}^2$ produces height variations of 20 nm [9, 19]. Therefore, on microscopic scale these effects can be neglected. Deposited films with $\kappa = 0.5$ are obtained at locations where energetic molecules hit the surface and films with $\kappa \lesssim 2$ at locations with reduced impact energy [9, 20–22]. One simple way to lower the impact energy is to reduce the duty cycle. Standard growth rates are between 1 and 500 \AA min^{-1} [9, 20]. The densities for fluorinated alkanes is reported with 1.6 to 2.2 g cm^{-3} [23, 24]. Surfaces with a $\kappa = 0.5$ are reported in [9] and [25]. Practical no chains ends through $-CF_3$ are reported for these surfaces and no degeneration effects happen for annealing temperature of up to 750 K[26].

2.3 Surface reactions

A surface reactions is characterized by at least one reactant absorbed at the surface. There are two possibilities for a surface reaction of two molecules:

- Eley-Rideal mechanism
- Langmuir-Hinshelwood mechanism.

In the Eley-Rideal mechanism the second molecule reacts directly from the gas phase with an absorbed surface atom. This is most likely a direct hit by the incoming particle. Due to the need for sufficient energy for this process this reaction channel is also called *hot atom mechanism*. For Langmuir-Hinshelwood both molecules are absorbed at the surface and get close to each other due to diffusion. This process is a thermal random with velocities much smaller than for Eley-Rideal. Therefore, this process has Eigentimes of the diffusion time-scale, which means millisecond.

One interesting feature of surface reactions is their reduced dimensionality. While in the plasma three-body-reactions like (B.1.25) to (B.1.27) are very unlikely, because a third body is needed to fulfill all conservation equations. The surface can act as the third reactant which is always present allowing much more efficient three-body-reactions.

The experimental observation of reduced mean energy of the incoming particle and increased fluorine concentration of the surface[9] can be understood as a consequence of changed fluorine atom losses at the surface. At low impact energy fluorine-rich surfaces are produced, because possibly less fluorine is ejected kinematically and more reactions are taking place. The $\text{CF}_2\cdot$ radical can establish a bond with the surface at these low energies and resulting in an fluorine enrichment of the surface. In contrast, at large impact energies fluorine is sputtered and $\text{CF}_2\cdot$ molecules are formed leaving the surface. Therefore, the surface can act as a radical sink or source for the plasma. Interestingly there is experimental evidence for both cases[27, 28].

For pure PTFE the separate chains are mostly not connected through covalent bonds. Major parts of the surface stability are therefore caused by other *intermolecular forces*. In the following section a brief description will be given.

2.4 Intermolecular forces

In the following section the mechanisms of interactions between molecules will be presented. Overall major contribution are from

- Repulsion
- Hydrogen bonding
- Keeson interaction
- Debye force
- London-dispersion force

Repulsion happens due to the Pauli principle which prevents the overlapping of electron orbitals. The molecules are forced apart to prevent this. The hydrogen bonds are formed by the effect of polarizing hydrogen atoms. The electron is pushed towards the bonding partner, the remaining positive hydrogen core charge is no longer shielded by the electron. This positive charge is attracted by electron pairs which are not in a bond with other atoms. This interaction will be illustrated for HF. In liquid HF chains are formed, because the fluorine atoms have free electron pairs. They act as an *acceptor*. Unlike water with two hydrogen atoms in the molecule, HF can only produce a single hydrogen bond. Therefore, very regular chains with practically no branching exist. Other acceptors can be Oxygen, Nitrogen or Sulfur. While the hydrogen bond in a $\text{F}-\text{H}\cdots\text{F}^-$ -ion is the strongest known hydrogen bond, only weak bonding is reported between hydrogen and fluorine bonded in polymers[29].

The Keeson interaction is caused by permanent electronic multipoles in the molecules. These multipoles favor a certain orientation towards each other. The minimum energy configuration for dipoles is a parallel linear configuration. The minimum energy configuration for quadrupoles is a T-shaped structure. Unlike Hydrocarbons, lacking any strong electronic moment, Fluorocarbon polymers have a strong charge polarization caused by the strong difference in electron negativity between fluorine and carbon or hydrogen. In case of HF this charge separation causes a dipole and quadrupole moment along the molecule axis. With the additional effects of dipole quadrupole interaction liquid HF chains are twisted like in Fig. 2.2.

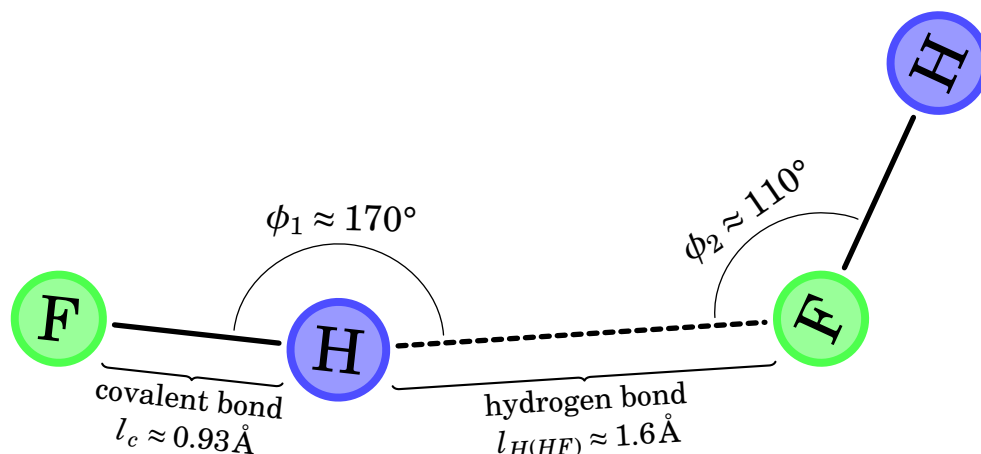


Figure 2.2: Angles and bond length for liquid fluorine hydrogen in the minimum energy configuration. This structure is mainly a result of the dipole and quadrupole moments.

A strong dipole like HF can also induce a multipole in a molecule without charge separation. This effect causes the Debye force. If one molecule is an ion this charge will also interact with the multipoles, both permanent and induced.

Additionally, the London-dispersion force is generated by correlated movements of the electrons in the interacting molecules. This effect also acts on non-polar molecules like hydrocarbons and its strength depends on the polarizability of the molecules. On the other hand, due to the strong electron negativity, fluorine is poorly polarizable and therefore the London-dispersion force will be weak between fluoropolymers. Despite the Keesom interaction all other contributions are non-additive, because changes in the surrounding of the molecule can affect all other contributions.

After the description of basic properties of carbon fluorine plasmas and amorphous films produced in such plasmas the method used in this work for simulating such systems will be introduced in the next chapter.



3

INTRODUCTION TO MOLECULAR DYNAMICS

Molecular dynamics (MD) is a technique in which the deterministic movements of particles is calculated solving the equation of motion. It was invented by Alder and Wainwright[30].

In this work MD allows to investigate and analyze particle surface interactions. Since the simulation is resolving the full microscopic-scale a direct simulation of the experiment is not possible due to run-time and memory restrictions. The strategy followed in this work is to create sample surfaces representing different experimental conditions and then to study the interaction of particles with these surfaces. Especially, calculation of sticking coefficients provide important input to global models and will be derived here. These sticking coefficients are the probability of a specie to get absorbed by the surface.

To compute the dynamics of such systems the complex interaction of particles is simplified. A usual method is to describe these interactions with an *interaction potential* (see 3.1), which includes the complete knowledge about the system in a parametric form. The complex problem of characterizing the system quantum mechanically is abstracted. This prevents the need to solve a huge system of complex equations.

Ab-initio MD requires the solution of the interaction potential at each time step using quantum mechanics. This is computationally not possible for the systems studied in this

work. Therefore, classical MD is used. All quantum mechanical effects are included in the parameterization of the interaction potential. A critical element is the obvious need for validation of the potentials, because nonphysical results can be obtained by a potential utilized beyond its limits.

The motion of the atomic nuclei is computed, following the Born-Oppenheimer-Approximation[31]. Due to the large difference between the masses of electrons and nuclei, the motion of both can be described separately. Assuming a much faster movement of the electrons each nucleus follows an effective potential. Hence, the electrons are not considered simplifying the problem and saving computation time. However, this makes it impossible to observe effects depending on the electronic structure like different reaction channels of radicals or ions of a molecule.

3.1 Interaction potentials

Interaction potentials determine the complete dynamics of the system. From these potentials Φ_i the forces acting on particles i are derived, e.g. the Coulomb force or Van-der-Waals-force caused by the electronic charge of the particles or their polarizability. From all potentials the total potential energy of the system can be calculated as the sum over the potential energies of all particles

$$E_{pot} = \sum_i \Phi_i. \quad (3.1.1)$$

To get the force acting on particle i in order to calculate its movement, the gradient of the potential is calculated

$$\vec{F}_i = -\vec{\nabla}_{\vec{r}_i} \Phi_i \quad (3.1.2a)$$

$$= m \cdot \vec{a}_i. \quad (3.1.2b)$$

This is correct for systems like the one studied in this work where potentials are only spatially depending, excluding e.g. velocity dependencies. Using the forces in the equation of motion numerical integration delivers the full dynamics of the system.

A central numeric task is the calculation of distances between particles. This determines the force and dynamics. Usually, a Taylor expansion of the interaction potential depending on the number of neighbors is used, the so-called "*m-body potential*"

$$\Phi_i = \Phi_i(\vec{r}_i) + \sum_{i \neq j} \Phi_{ij}(\vec{r}_i, \vec{r}_j) + \sum_{i \neq j, k} \Phi_{ijk}(\vec{r}_i, \vec{r}_j, \vec{r}_k) + \dots \quad (3.1.3)$$

The first expansion term includes contribution from external fields. A potential consisting only of the first two terms is termed as "*pair-potential*". The pair potentials only depend on the distance between particles (further noted with $\vec{r}_{ij} = \vec{r}_i - \vec{r}_j$ and $r_{ij} = |\vec{r}_i - \vec{r}_j|$), while more advanced potentials include properties like the particle density or the angle between three particles. The main problem of higher order potentials are their increasing computational costs, which grows with expansion order. For a 3-body potential it scales with N^3 , where N is the number of particles in the simulation.

These potentials are capable to describe at least some aspects of relatively small molecules like water with a Lennard-Jones potential (see Fig. 3.1). The potential is only depending

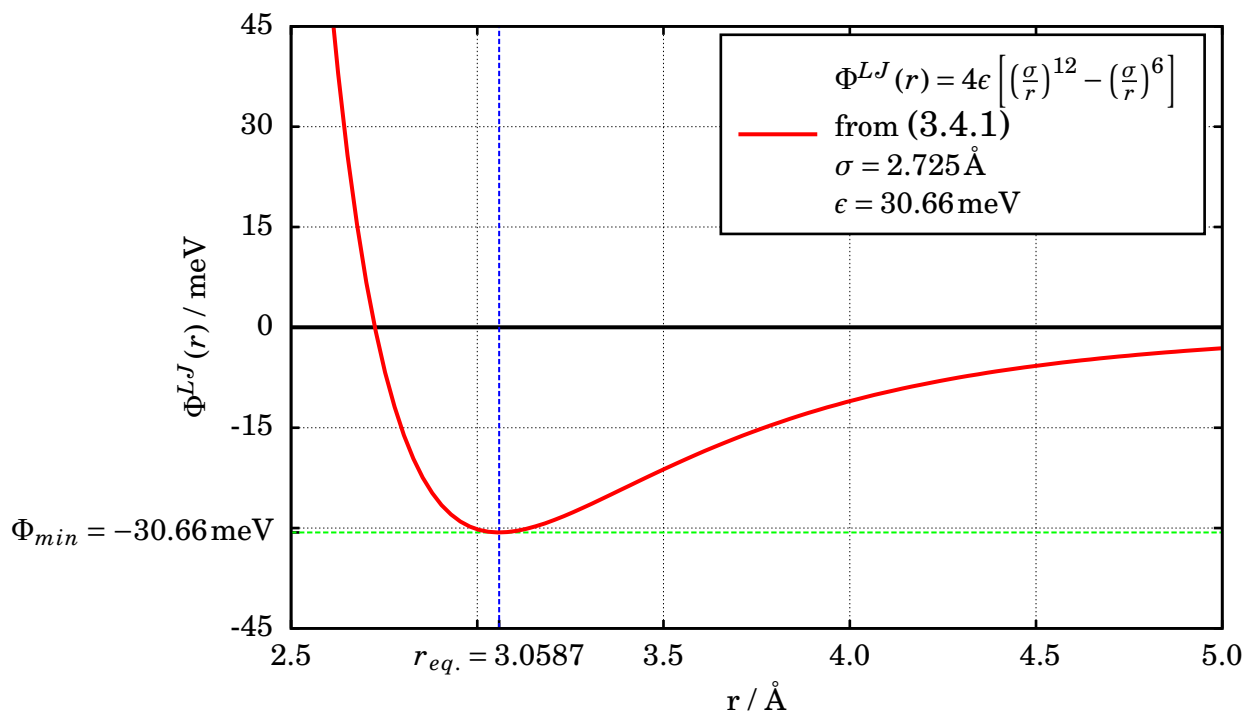


Figure 3.1: Pair potential to describe the intermolecular interactions between water molecules from [32]. Due to the strong hydrogen bonds in water for an intermolecular potential the minimum is quite deep.

on *distance*. *Angular* effects like in Fig. 2.2 can not be reproduced. The simulated structure will therefore be different from the structure of real water. For more complex cases like the bonding in carbon molecules, it is necessary to include higher body-terms.

There is a huge number of interaction potentials existing, specifically so-called *force-fields*. These are empirically fitted potentials, usually using only harmonic or semi-harmonic approximation. They are very popular for drug design and biological systems due to their simplicity and small computational costs. One major short-coming in using such force-fields is their incorrect description of reaction dynamics due to their simplified form.

In the following section a more complex potential description overcoming these shortcomings is presented. The *AIREBO-potential* will be derived from its ancestor, the *Tersoff-potential*.

3.2 Tersoff Potential

In this section the so-called “*Tersoff-Potential*” will be introduced. The aim of this work is to understand the reaction of molecule consisting of fluorine and carbon with surfaces also consisting of these constituents. To describe such systems a potential formulation originally developed by J. Tersoff for silicon is adapted.

Abell [33] derived a general expression for the binding energy, which Tersoff [34] used as

pair potential

$$\Phi_{ij} = \left[\alpha_{ij} \cdot V_R(r_{ij}) + \tilde{b}_{ij} \cdot V_A(r_{ij}) \right]. \quad (3.2.1)$$

The key feature of this potential (3.2.1) is the invention of the so-called *bond-order term* \tilde{b}_{ij} . Its influence is illustrated in figure 3.2.

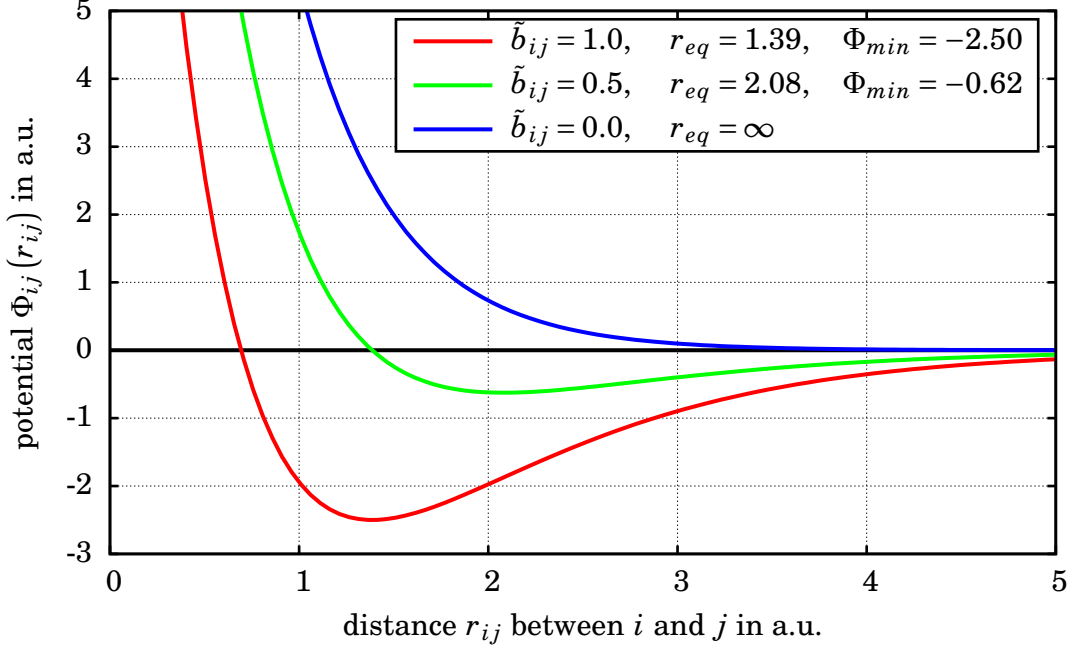


Figure 3.2: Influence of the bond-order term \tilde{b}_{ij} introduced in eq. (3.2.1). Depending on \tilde{b}_{ij} the potential minimum or bond energy as well as the equilibrium distance is varied. Due to \tilde{b}_{ij} depending on various parameters (see eq. (3.2.2)) certain configurations, like a diamond-like structure, can be achieved.

The bond-order term is determined by the local environment, which includes implicitly three or higher-body interactions. This makes a computational cheap pair-potential sufficient for the description of a complex problem. Therefore, \tilde{b}_{ij} is not a constant, but must be calculated for *every* interaction in *each* time step.

Tersoff[35] proposed the following form

$$\begin{aligned} \tilde{b}_{ij} &= \left(1 + \beta^n \zeta_{ij}^n \right)^{-\frac{1}{2n}}, \\ \zeta_{ij} &= \sum_{k \neq i,j} f_C(r_{ik}) g_C(\vartheta_{ijk}) \exp \left[\lambda_3^3 (r_{ij} - r_{ik})^3 \right], \\ g_c(\vartheta) &= 1 + \frac{c^2}{d^2} - \frac{c^2}{d^2 + (h - \cos \vartheta)^2}, \end{aligned} \quad (3.2.2)$$

where ϑ_{ijk} is the angle between \vec{r}_{ij} and \vec{r}_{ik} . The parameters c , d , h , β , n and λ_3 are used in the fitting procedure, where they are chosen such that the resulting potential can reproduce known properties like stable structures or phonon energies. It should be noted,

that $\tilde{b}_{ij} \neq \tilde{b}_{ji}$ due to different environments around i and j . As a consequence binding energies can be non-uniform between two atoms. This bond-order term can be further modified, as will be shown in Sec. 3.3.

The Tersoff potential consists of an attractive V_A and a repulsive part V_R , which are modified by the functions f_C and \tilde{b}_{ij} . Following Abell these functions are chosen with exponential decay:

$$V_R(r_{ij}) = f_C(r_{ij})A \exp(-\lambda_1 r_{ij}), \quad (3.2.3a)$$

$$V_A(r_{ij}) = -f_C(r_{ij})B \exp(-\lambda_2 r_{ij}). \quad (3.2.3b)$$

The interactions are mostly acting on a short-range. Computational time can be saved if less interactions must be calculated. Only the nearest neighbors like the first shell of neighbors are considered. This is achieved via a *cut-off function* f_C like

$$f_C(r_{ij}) = \Theta(r_{ij}^{\min} - r_{ij}) + \Theta(r_{ij} - r_{ij}^{\min}) \Theta(r_{ij}^{\max} - r_{ij}) \frac{1}{2} \left[1 + \cos \left(\pi \frac{r_{ij} - r_{ij}^{\min}}{r_{ij}^{\max} - r_{ij}^{\min}} \right) \right] \quad (3.2.4)$$

which smooths the potential to zero in the transition region from r_{ij}^{\min} to r_{ij}^{\max} leading to no further interactions between these atoms further apart. In the original Tersoff ansatz this region was uniform for all different interactions. As will be seen in the following section 3.3, this cut-off region can be dependent on the interacting species. This is indicated by the ij index. The cut-off distance depends on the species of atom i and j .

Unlike classical force-fields, where bounds are approximated with harmonic oscillators resulting in very large walls on both sides, the smoothing term combined with the decay functions (3.2.3a) and (3.2.3b) enables breaking and forming of bounds as long as sufficient kinetic energy is available. Consequently, the depth of the potential is fitted to known bond-dissociation energies. This does not mean a Tersoff-like potential is always superior to a classical force-field, because the inclusion of exponential and cosine terms is computationally much more costly but also as the neighbors of an atom can change, regular checks of the neighbor list are necessary (see chapter 4 for further details). For studies of large molecules, where no bonds are formed or broken, classical force-fields are the right choice (e.g. for non-reactive fluorine carbon systems[23]).

In the form of a_{ij} proposed by Tersoff[35] this term is only different from $\simeq 1$ outside the first shell of neighbors, which is excluded by the cut-off function $f_C(r_{ij})$. Therefore, in most applications of the Tersoff-potential a_{ij} it is assumed as 1 and is not further considered.

The overbinding of radicals may occur in the Tersoff potential, e.g. the bonds to an atom with low coordination number, say three for a carbon atom, will be interpolated between single and double bonds. Free $2p$ orbitals at the ligand are not considered because in the Tersoff-potential no difference exists between single, double and triple bonds. Likewise conjugated and non-conjugated double bonds are treated the same, although they will have different binding energies.

For hydrogen-carbon systems an extension of Tersoff potential was suggested by Brenner in 1990[36] through the *reactive empirical bond-order potential* (REBO-potential) which will be specified in following.

3.3 Reactive Empirical Bond-Order Potential

Brenner switches from a calculation of the energy in eq. (3.2.1) *based on atoms* to a calculation *based on bonds*

$$\Phi_i = \sum_{j(>i)} V_R(r_{ij}) - b_{ij} V_A(r_{ij}) \quad (3.3.1)$$

with

$$\begin{aligned} b_{ij} &= \frac{\tilde{b}_{ij} + \tilde{b}_{ji}}{2} \\ &= \frac{b_{ij}^{\sigma-\pi} + b_{ji}^{\sigma-\pi}}{2}. \end{aligned} \quad (3.3.2)$$

To achieve that a bond will have the characteristics of a double or triple bond the term $\pi_{ij}(\cdot)$ is added, if the local coordination of the bond-forming carbon atoms allows it. This term attributes to the radical and conjugate behavior of the system. As the electrons are completely neglected the effect of conjugation, a quantum mechanically effect caused by delocalized electrons, is treated in purely geometrical manner

$$b_{ij} = \frac{b_{ij}^{\sigma-\pi} + b_{ji}^{\sigma-\pi}}{2} + \pi_{ij}^{rc}. \quad (3.3.3)$$

Likewise, π_{ij}^{rc} is determined by a tricubic spline $F_{ij}(N_i^{(t)}, N_j^{(t)}, N_{ij}^{conj})$ [37]. The arguments of this spline are the total number of neighbors for both bond forming atoms $N_i^{(t)}, N_j^{(t)}$ and the number of carbon neighbor atoms for both carbon atoms N_{ij}^{conj} . N_{ij}^{conj} attributes to the conjugated state of the bond (see eq. (3.3.7)). The spline is fitted to known molecular structures and binding energies.

Here, N_x^t represents the total number or neighbors for atom x , which is derived via

$$N_x^{(t)} = N_x^{(H)} + N_x^{(C)}, \quad (3.3.4)$$

$$N_x^{(H)} = \sum_l^{hydrogen} f_{xl}(r_{xl}) \quad (3.3.5)$$

$$N_x^{(C)} = \sum_l^{carbon} f_{xl}(r_{xl}) \quad (3.3.6)$$

where for $f_{xl}(r_{xl})$ the same switching function (3.2.4) is used. However, not a single cut-off area is taken into account, but for each different species combination an individual cut-offlength is defined.

In the parameter N_{ij}^{conj} for carbon atoms the conjugation state is specified in the following way

$$N_{ij}^{conj} = 1 + \left[\sum_{k \neq i,j}^{carbon} f_{ik}(r_{ik}) F(x_{ik}) \right]^\delta + \left[\sum_{l \neq i,j}^{carbon} f_{jl}(r_{jl}) F(x_{jl}) \right]^\delta \quad (3.3.7)$$

3.3. REACTIVE EMPIRICAL BOND-ORDER POTENTIAL

with

$$F_{ik} = \Theta(2 - x_{ik}) + \Theta(x_{ik} - 2)\Theta(3 - x_{ik}) \left[\frac{1 + \cos(2\pi(x_{ik} - 2))}{2} \right] \quad (3.3.8)$$

and

$$x_{ik} = N_k^{(t)} - f_{ik}(r_{ik})$$

The bond order term from (3.2.2) is transformed to

$$b_{ij}^{\sigma-\pi} = \left[1 + \sum_{k(\neq i,j)} f_c(r_{ik})g_c(\cos \vartheta_{ijk}) \exp^{\lambda_{ijk}[(r_{ij}-R_{ij}^e)-(r_{ik}-R_{ik}^e)]} + P_{ij} \left(N_i^C, N_i^H \right) \right]^{-\delta} \quad (3.3.9)$$

The differences to Eq. (3.2.2) are:

- $n = 1$
- the order of $r_{ij} - r_{ik}$ in the exponential function ζ_{ij} is decreased to one
- a correction term P_{ij} added.

P_{ij} describes the difference of the bond energy to the solid state-case. This term describes the possibility to form double or triple bonds in carbon. For a better description of such bonds in the fitting procedure additional molecules with double and triple bonds are included.

In 2001 Brenner et al. published an extended version of this potential[38]. The main differences to the first generation potential are discussed in the following.

Most notable is the change of the repulsive and attractive pair-terms (3.2.3a) and (3.2.3b) to the form of

$$V_R(r_{ij}) = f_{ij}(r_{ij}) \left(1 + \frac{Q_{ij}}{r_{ij}} \right) A_{ij} \exp(-\alpha_{ij} r_{ij}), \quad (3.3.10a)$$

$$V_A(r_{ij}) = -f_{ij}(r_{ij}) \sum_{n=1}^3 B_{ij}^{(n)} \exp(-\beta_{ij}^{(n)} r_{ij}), \quad (3.3.10b)$$

which were chosen by “*trial and error*”[39] to produce a more accurate potential. More fitting parameters allow to consider more bond lengths, energies and force constants. The resulting potential together with the extension for fluorine by Jang[40] is shown in Fig. 3.3. Jang’s coefficients are taken as they are also include hydrogen, not like the one from Tanaka[41], which only includes carbon and fluorine. These potential curves match the exact curves in reality but are more an approximation[42].

Further changes are in the term π_{ij}^{rc} in eq (3.3.3) representing the radical character of a bond to which a further term π_{ij}^{dh} for calculating the influence of the dihedral angle in a carbon-carbon double bond is added. This results in the new bond-order term

$$b_{ij} = \frac{b_{ij}^{\sigma-\pi} + b_{ji}^{\sigma-\pi}}{2} + \pi_{ij}^{rc} + \pi_{ij}^{dh}. \quad (3.3.11)$$

While in principle the terms describing the σ and π bonds $b_{ij}^{\sigma-\pi}$ from Eq. (3.3.9) remains the same, in the exponential term the distance dependence is included in the variable

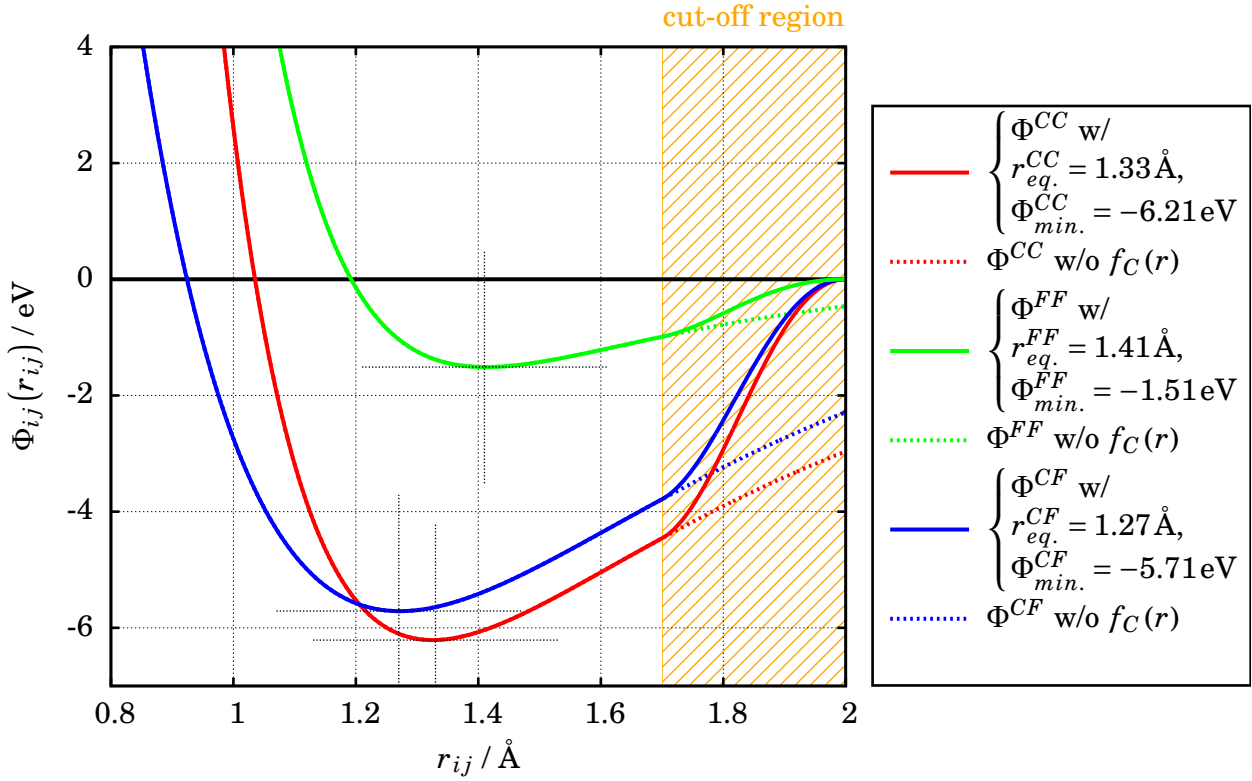


Figure 3.3: The intramolecular part of the used potential ((3.3.1) with (3.3.10a) and (3.3.10b)). Here the carbon-carbon, fluorine-fluorine and carbon-fluorine interactions are plotted on a per-bond basis. As the bond order term is shown with $b_{ij} = 1$ the form of the potential will vary exceedingly depending on the researched structure. Also one can see the strong influence of the switching function.

and δ is chosen as 1/2 leading to

$$b_{ij}^{\sigma-\pi} = \left[1 + \sum_{k(\neq i,j)} f_c(r_{ik}) g_c(\cos \vartheta_{ijk}) \exp^{\lambda_{ijk}} + P_{ij}(N_i^C, N_i^H) \right]^{-\frac{1}{2}} \quad (3.3.12)$$

with

$$\lambda_{jik} = \sum_{x=H,\dots} 4\delta_{ix} \left[r_{ij} - r_{ik} + \sum_{y=C,H,\dots} \rho_{yx} (\delta_{ky} - \delta_{jy}) \right]. \quad (3.3.13)$$

The correction term $P_{ij}(N_i^C, N_i^H)$ is necessary to take into account different chemistry of bonds depending on the density of specific species. P_{ij} is a cubic spline through provided data points. While in the original papers[38] only the interaction of two species, carbon and hydrogen atoms, is considered, increasing the dimensionality of this cubic spline allows to add more species like fluorine [40]. All other terms depend only on the species of two atoms or the total density of atoms in the direct neighborhood. Therefore, $P_{ij}(N_i^C, N_i^H)$ has to include the number of Fluorine atoms to $P_{ij}(N_i^C, N_i^H, N_i^F)$.

In this expression the angular dependence is changed from eq. (3.2.2) to

$$g_c(\cos \vartheta) = G_C(\cos \vartheta) + Q(N_i^{(t)}) [\gamma_C(\cos \vartheta) - G_C(\cos \vartheta)] \quad (3.3.14)$$

3.3. REACTIVE EMPIRICAL BOND-ORDER POTENTIAL

in which G_C is a sixth-order polynomial spline. The low-coordination structure γ_C , which is obtained through fitting of small angle configurations, is taken into account by the local coordination for *atom i*

$$N_i^{(t)} = N_i^C + N_i^H + \dots \quad (3.3.15)$$

and the switching function

$$Q_i(N_i^{(t)}) = \Theta(3.2 - N_i^{(t)}) + \Theta(N_i^{(t)} - 3.2) \Theta(3.7 - N_i^{(t)}) \frac{1 + \cos\left[2\pi(N_i^{(t)} - 3.2)\right]}{2} \quad (3.3.16)$$

The third term in eq. (3.3.3) describes the radical and conjugated character of the bond and is given via a tricubic spline fit through the number of hydrogen and carbon neighbors and eq. (3.3.7), in which δ is changed to $\delta = 2$. Also the fitting species are changed so different data points are included.

A complete new addition is the fourth term π_{ij}^{dh} specifying the dihedral limitation of a carbon-carbon double bond.

$$\pi_{ij}^{dh} = T_{ij}(N_i^{(t)}, N_j^{(t)}, N_{ij}^{conj}) \left[\sum_{k(\neq i,j)} \sum_{l(\neq i,j)} (1 - \cos^2 \vartheta_{ijkl}) f_{ik}^C(r_{ik}) f_{jl}^C(r_{jl}) \right] \quad (3.3.17)$$

with

$$\vartheta_{ijkl} = \frac{\vec{r}_{ji} \times \vec{r}_{ik}}{\|\vec{r}_{ji} \times \vec{r}_{ik}\|_2} \cdot \frac{\vec{r}_{ij} \times \vec{r}_{jl}}{\|\vec{r}_{ij} \times \vec{r}_{jl}\|_2} \quad (3.3.18)$$

The parameters are fitted to various species, structures and reactions, which are often obtained via first principle calculations or measurements, to get a potential as accurate as possible. Up to now only *inter-molecular* effects are included, but no *intra-molecular* effects. Therefore, a pure reactive bond order potential is most suitable for cases, where solid state or high connected phases are described. For weakly bond molecules like films or the interaction between layers in graphite this limitation may lead to unphysical results. Electronic force contribution due to charge distribution effects need to be included.

A computationally cheap and also established method are the so called *12-6 Lennard-Jones potentials* like introduced in section 3.1. Here, the attractive term of a dipole scaling with r^{-6} acts against a repulsive term scaling with r^{-12} , which represents the repulsive forces of overlapping orbitals. As this potential alone would prevent a transition from the large distance of an *intermolecular* interaction to the short distance of an *intramolecular* interaction, it is necessary to handle switching of the Lennard-Jones-Potential. This is determined by the current bonding state specified by the bond-order-term and the position relative to each other in a molecule for the two interacting atoms. In the following section the inclusion of this *12-6 Lennard-Jones potentials* into the reactive bond order will be presented leading to the *adaptive intermolecular bond order potential*.

3.4 Adaptive Intermolecular Reactive Empirical Bond Order Potential

To include the intermolecular interactions in the reactive empirical bond-order (REBO) potential Stuart, Tutein and Harrison[43] proposed the inclusion of a potential based on a 6 – 12 Lennard-Jones potential. The resulting potential is called *adaptive intermolecular reactive bond order-potential* (AIREBO) and will be presented in the following. In the original AIREBO-potential an additional term is added to contribute to the torsional limitation of specific carbon-carbon bonds.

The used 6 – 12 Lennard-Jones potential is

$$\Phi_{ij}^{LJ}(r_{ij}) = 4\epsilon_{ij} \left[\left(\frac{\sigma_{ij}}{r_{ij}} \right)^{12} - \left(\frac{\sigma_{ij}}{r_{ij}} \right)^6 \right] \quad (3.4.1)$$

where the values are given in Table B.2 and are chosen from [43] for the *C–H*-interaction and from [40] for the C-F and H-F interaction. This is the same potential but with different coefficients like the one for water in Fig. 3.1. While the form remains identical the other coefficients shift the equilibrium distance and scale the potential depth. It should be noted that the binding energy or more precisely the potential minimum for the interaction of only two atoms is only a fraction of the binding energy of an intermolecular bond between the two (like a factor 10^{-3}). But due to the minimum located at greater distance, each atom can have more intermolecular interacting neighbors leading to effective binding energies well above the kinetic energy of a molecule.

The form of eq. (3.4.1) tends to infinity for $r \rightarrow 0$. Because σ_{ij} is normally larger than the normal bond-length without further terms one would get a too high barrier preventing the formation and breaking of bonds. Due to the reactive behavior of the system there exist cases, where the Lennard-Jones potential has to be reduced. Such cases with small Lennard-Jones interactions are:

1. distance so small making the formation of a bond possible,
2. low coordination number with the possibility of forming a bond,
3. close atoms in the same molecule.

These requirements are fulfilled by the following term

$$\mathcal{E}_{ij}^{LJ} = C_{ij} \Phi_{ij}^{LJ}(r_{ij}) \left[1 - f_{LJ}(t_r(r_{ij})) \cdot \left[1 - f_{LJ}(t_b(b_{ij}^*)) \right] \right] \quad (3.4.2)$$

in which the first request is implemented by the switching function depending on the distance $f_{LJ}(r_{ij})$, the second request by the switching function depending on a hypothetical $f_{LJ}(b_{ij}^*)$ and the third request by the connectivity switch C_{ij} . The derivation of these terms will be explained in the following (for visualization see fig. 3.4).

The first case is attributed to a distance-dependent switch, which slightly differs from eq. (3.2.4) in the original REBO-potential (see also Sec. 5.2)

$$f_{LJ}(t) = \Theta(-t) + \Theta(t)\Theta(1-t) [1 - t^2(3-2t)] \quad (3.4.3)$$

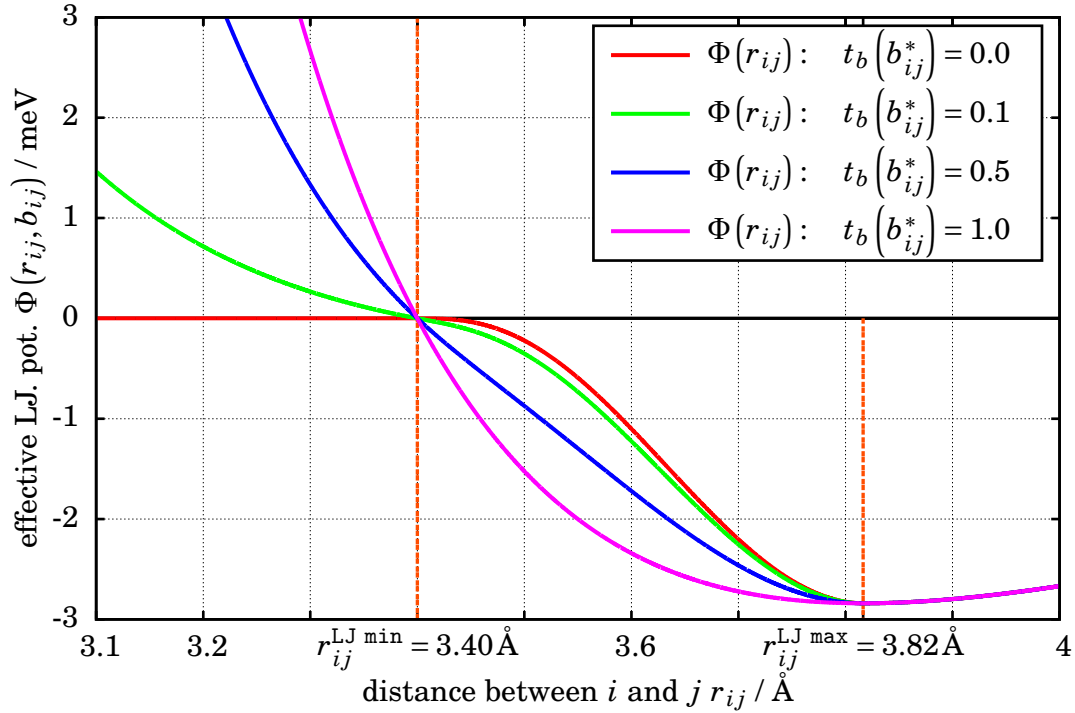


Figure 3.4: Influence of the bond-order term on the Lennard-Jones part of the potential

with transition region r_{ij}^{\max} and r_{ij}^{\min} normalized to the interval $[0, 1]$

$$t_r(r_{ij}) = \frac{r_{ij} - r_{ij}^{\text{LJ min}}}{r_{ij}^{\text{LJ max}} - r_{ij}^{\text{LJ min}}}. \quad (3.4.4)$$

Here, (3.4.4) inserted in the switching function (3.4.3) leads to an unperturbed Lennard-Jones potential for distances greater than r_{ij}^{\max} . In the transition region the Lennard-Jones potential goes to zero close to r_{ij}^{\min} . The two other request 2) and 3) can modify this.

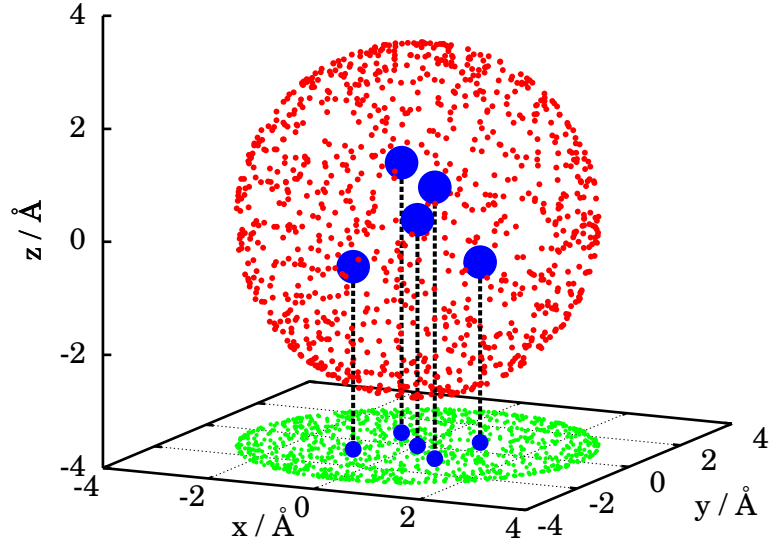
The borders of the transition area are defined as

$$r_{ij}^{\text{LJ min}} = \sigma_{ij} \quad \text{and} \quad r_{ij}^{\text{LJ max}} = 2^{\frac{1}{6}} \sigma_{ij} \quad (3.4.5)$$

from the potential minimum. This leads to an unperturbed potential minimum and also a continuous second derivative at r^{\min} .

As already pointed out in Sections 3.3 and 3.2 the number of bonds is limited in Tersoff-like potentials like the AIREBO-potential by the bond-order term b_{ij} from eq. (3.3.3). This term is multiplied with the attractive component of the potential and includes the local coordination number of two interacting atoms. It is high, if both atoms have the possibility to form further bonds, causing this way a strong attraction between the two. It is low, if a bond formation is unlikely. Since the second request is the switching-off of the repulsive barrier for cases with low local coordination number, as the formation of a bond between two radicals is likely, another switching function $f_{LJ}(t_b(b_{ij}^*))$ is added to

Figure 3.5: Estimation of the characteristic bond-order term for reactive (CF and CF₃) and non-reactive species (CF₄ as shown in the right). The red dots are random position at which the hypothetical bond-order term (3.4.6) is evaluated.



the Lennard-Jones potential. Here, for the hypothetical term

$$b_{ij}^* = b_{ij} \Big|_{r_{ij} = r_{ij}^{\min}} \quad (3.4.6)$$

the local coordination is calculated. It is assumed that both radicals are separated by r_{ij}^{\min} . With

$$t_b(b_{ij}^*) = \frac{b_{ij}^* - b_{ij}^{\min}}{b_{ij}^{\max} - b_{ij}^{\min}} \quad (3.4.7)$$

the barrier is absent for bond-order terms greater than b_{ij}^{\max} and full active for bond-order terms smaller than b_{ij}^{\min} . In between a smooth transition is achieved via the switch-off function (3.4.3). As the bond-length and bonding characteristics are type-dependent for every combination the maximum and minimum have to be determined like it was done by Stuart et al. [43]. They fitted the C-H interaction by calculating the bond-order term for a hydrogen atom approaching a methane and a methyl radical. From the first case, where a reaction is very improbable, the lower limit of $b_{ij}^{\min} = 0.75$ is derived, while the highly reactive second case leads to the upper limit of $b_{ij}^{\max} = 0.90$. A complete list of all used parameters is given in table B.2.

At last to fulfill the third request of no *intermolecular* interaction for atoms located “near” to each other in the same molecule, the term

$$C_{ij} = 1 - \max\{w_{ij}(r_{ij}), w_{ik}(r_{ik})w_{jk}(r_{jk}) \forall k, w_{ik}(r_{ik})w_{kl}(r_{kl})w_{lj}(r_{lj}) \forall k\} \quad (3.4.8)$$

is included in which $w_{ij}(r_{ij}) = f_C(r_{ij})$ is defined by eq. (3.2.4). By this, the switching function (3.4.3) from the Lennard-Jones potential is no longer used but the switching function of the REBO-potential. With (3.4.8) atoms with two, one or no intermediate neighbors do not longer interact. In these cases C_{ij} becomes zero and with it the whole *intermolecular* potential.

This completes the description of the interaction potential and the simulation technique used in this work. The next chapter will present further details about the numerical implementation.



4

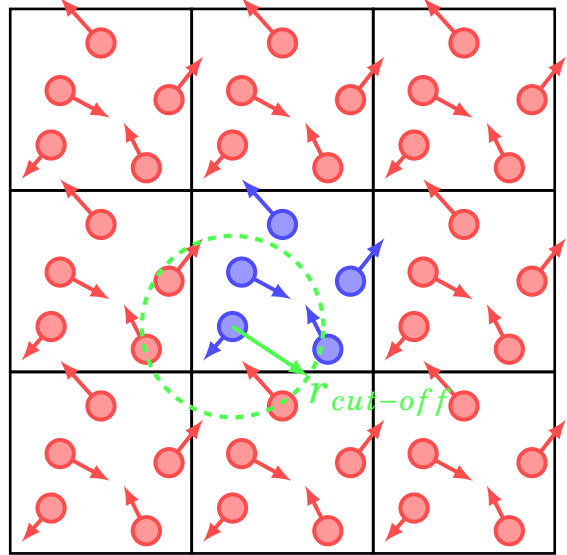
NUMERICAL IMPLEMENTATION

This chapter will contain some details about the implementation of numerical methods used in the simulation. The open source *Large-scale Atomic / Molecular Massively Parallel Simulator (LAMMPS)* package[44] from Sandia National Laboratories is used for the work. An AIREBO-potential for hydrogen-carbon systems was already existing which has been extended in this work to include fluorine. LAMMPS has its own input-file format, which can be used for setting different parameters and options without recompilation of the code.

As mentioned in section 3.1, the computational effort scales for pair potentials with N^2 (N - number of investigated particles). This is mainly caused by the need of checking the distances between all particles and to calculate the forces between them. With the use of the range limiting *cut-off functions* like eq. (3.2.4) the total number of force calculations is reduced, nevertheless all inter-atomic distances still have to be calculated. An improvement can be achieved through the construction of *neighbor-lists* and the inter-atomic distance is calculated only for the neighbors from this list. This list has to be updated after a certain amount of time to prevent the approach of two non-interacting particles. In the simulation this neighbor-list is updated every tenth time step and only the particles within the *cut-off length* r_{ij}^{\max} plus a security distance of 0.5 Å are included. This security distance has to be larger if higher velocities occur in the system. Alternatively, the number of time steps between list updates can be reduced.

Periodic boundary conditions are applied in all three dimensions during the generation of the bulk and later removed in z-direction to get the surface. Such boundary conditions are realized by the introduction of *ghost atoms*. These are shifted copies of the original

Figure 4.1: Scheme of the applied periodic boundaries. The blue atoms are the real atoms, while the red ones are their shifted copies. With no periodicity all atoms would cluster together in one big cube. Additionally to prevent self-forces and other defects the box size has to be at least two times the largest cut-off length.



atoms of which every real atom creates up to twenty six in a three dimension and up to eight copies in a two dimension periodic system outside the periodicity box. Ghost atoms interact as if they were real and at the end of the time step their forces are added to their associated real atoms, which are then integrated. At the beginning of the next time step new ghost atoms are created. Due to the addition of ghost atom a minimum requirement for the size of the simulation box is needed. If the simulation box would be

$$l_x|l_y(|l_z) < 2 \cdot r_{\text{cut-off}} \quad (4.0.1)$$

an atom would not only interact with the real atom or its copy but eventually with both. As the forces to the real atom and its copy would be anti-parallel they would compensate, at least partly, resulting this way in a too small net force.

The parameters from Jang[40] are used for the interaction potential. This includes especially the cut-off length for the Lennard-Jones interaction of

$$r_{\text{cut-off}} = 3.0 \cdot r_{cc}^{\text{LJ}} \approx 11.5 \text{ \AA}. \quad (4.0.2)$$

Therefore, a minimum length for the box size

$$l_{\text{min.}} = 25 \text{ \AA} \quad (4.0.3)$$

was chosen.

The ghost atoms have also another application. The whole simulation box is split into domains. These domains are each managed by different processors. The atoms managed by other processors are now also treated as ghost atoms, so at the end of the time step the forces have to be communicated. Thereby for communication the internal structure is sometimes ordered after the master slave principle. This limits the number of processors, which can be used effectively in parallel mode. The version of LAMMPS used in the present work (released on the 7th April 2011) has no load-balancing capabilities and this is a shortcoming, if one aims to simulate an asymmetric distribution of atoms (like a surface with a free space above).

Further updates in LAMMPS were incorporated in the version used in the present work through the public available git-tree[45], e.g. some changes to “pair_airebo.cpp”. In this

file a carbon-hydrogen AIREBO-potential is implemented and the basic idea to include a three species potential was introduced by Bandelow with the generation of constants e.g. for the splines. Some improved book-keeping algorithm was tried in the potential calculation through caching the distances between particles to prevent multiple calculations per time step. This turned out to be unsuccessful, in contrast to the rearranging in the switching functions and some other simplifications (see also section 5.2).

LAMMPS uses an integrator based on the *Velocity-Verlet algorithm*, although it would have been logical to use other higher order integration methods allowing possibly larger time steps. Due to the fact the base time step of the simulation is limited by physics (see section 4.2), not by numerics and because it would be very time-consuming to change the integrator in LAMMPS it was not done in the present work. The integrator used in LAMMPS will be briefly described in the next section followed by the estimation of time step. Additionally, a description is given about controlling methods of temperature and pressure. At the end of this chapter some remarks are made about other changes implemented into the code.

4.1 Velocity-Verlet Algorithm

Integration of the equation of motion is done at every time step for every particle with the Velocity-Verlet algorithm. This algorithm consists of four steps:

1. Calculation of position by

$$\vec{x}(t + \Delta t) = \vec{x}(t) + \vec{v}(t) \cdot \Delta t + \frac{1}{2} \vec{a}(t) (\Delta t)^2 \quad (4.1.1)$$

2. Calculation of velocity after one half time step

$$\vec{v}\left(t + \frac{\Delta t}{2}\right) = \vec{v}(t) + \frac{\vec{a}(t) \Delta t}{2} \quad (4.1.2)$$

3. Calculation of acceleration $\vec{a}(t + \Delta t)$ with calculating the force F_i for every particle
4. Calculation of velocity after the full time step

$$\vec{v}(t + \Delta t) = \vec{v}\left(t + \frac{\Delta t}{2}\right) + \frac{\vec{a}(t + \Delta t) \Delta t}{2} \quad (4.1.3)$$

The Velocity-Verlet algorithm has the advantage of velocities and positions being time-synchronised in contrast to the half time step shifted leap frog method[46]. As a consequence the kinetic and potential energies are synchronized as well and no interpolation is needed. This way, no further error is introduced and one gets as a result better numerical stability. A disadvantage of this algorithm is the half time step shifted velocity for the force/acceleration calculation. Therefore, it is a bad choice for problems which include viscosity. As a second-order method the accuracy is not as good as a higher order algorithm, like the fourth or fifth order Runge-Kutta. However, this is compensated by its lower computing cost. Also, a very attractive feature of this integrator is that it conserves energy and momentum.

4.2 Estimation of the time step

The choice of the time step for MD is critical due to the request for a balance between numerical accuracy and needed run-time. A large time step reduces the number of potential calculations needed to simulate the desired time, because every potential call is computationally very costly. No arbitrary large time step can be chosen because a larger time step will lead to larger integration errors. By defining a maximal acceptable error, the time step can be derived from the current largest velocity in the system.

This maximum error defines also the accepted deviations from the conservation equations of energy and momentum. These deviations should be so small that their impact on the system is still negligible. To guarantee that a particle is interacting with the proper potential and to avoid that it will penetrate through a potential wall due to numerical errors, it is necessary to estimate the largest acceptable time step. An appropriate time step will guarantee a smoother change of the force and prohibit sudden artificial accelerations of some particles which could cause instabilities in the molecules. One common technique is a Taylor expansion around the equilibrium distance r_{eq} . Since in equilibrium the net force is zero the first derivative will vanish and the resulting form can be approximated by a harmonic oscillator:

$$\tilde{\Phi}(r) = \Phi_{min.} + \frac{1}{2} \left. \frac{\partial^2 \Phi(r)}{\partial r^2} \right|_{r=r_{eq.}} + O(r^3) \quad (4.2.1a)$$

$$\stackrel{!}{=} V_0 + \frac{m \cdot \omega^2}{2} \cdot (r - r_{eq.})^2 \quad (4.2.1b)$$

resulting in the period of oscillation $\tau = \frac{2 \cdot \pi}{\omega}$

$$\tau = 2\pi \cdot \sqrt{\frac{m}{\left. \frac{\partial^2 \Phi(r)}{\partial r^2} \right|_{r=r_{eq.}}}} \quad (4.2.1c)$$

Assuming for the potential (3.3.1) a bond order term of $b_{ij} = 1$ one gets with (3.3.10a) and (3.3.10b) within the cut-off region the second derivative for the intra-molecular interaction:

$$\begin{aligned} \frac{\partial^2 \Phi_{ij}}{\partial r_{ij}^2} = & A_{ij} \left[\alpha_{ij}^2 + \frac{\alpha_{ij}^2 Q_{ij}}{r_{ij}} + \frac{2\alpha_{ij} Q_{ij}}{r_{ij}^2} + \frac{2Q_{ij}}{r_{ij}^3} \right] \exp(-\alpha_{ij} r_{ij}) \\ & - \sum_n B_{ij}^{(n)} \left(\beta_{ij}^{(n)} \right)^2 \exp\left(-\beta_{ij}^{(n)} r_{ij}\right) \end{aligned} \quad (4.2.2)$$

With the coefficients from Table B.1 the periods for the carbon-carbon and the hydrogen-hydrogen interaction are

$$\tau_{CC} \approx 40 \text{ fs} \qquad \tau_{HH} \approx 11 \text{ fs} \quad (4.2.3)$$

Doing the same for the Lennard-Jones part of the potential one gets

$$\tilde{\Phi}^{LJ}(r) = \epsilon_{ij} + \frac{18 \cdot 2^{\frac{2}{3}}}{\sigma_{ij}^2} \cdot \epsilon_{ij} (r - r_{eq.})^2 + O(r^3) \quad (4.2.4a)$$

$$\Rightarrow \tau_{CC} \approx 3.7 \text{ ps.} \quad (4.2.4b)$$

As a rule of thumb the shortest time resolved in the system should be at least ten times larger than the time step. Therefore, a time step of the order of $\Delta t = 1$ fs should be used. Unfortunately, this assumption is only valid around the point of equilibrium. Consequently, this time step is only sufficient for cases without bond formation or higher temperatures. In these cases smaller time steps are needed to resolve the dynamics adequately. One exception is the binary collision simulation presented in chapter 5.1 where the atoms are accelerated by the whole potential. Likewise an adequate estimate of the transformed kinetic energy (B.1.1) can be obtained from the potential depth

$$v = \sqrt{\frac{2\Phi_{\text{min. CC}}}{m}} \approx 0.071 \text{ \AA fs}^{-1}. \quad (4.2.5)$$

Assuming to need at least one hundred time steps crossing the interaction region with a width of about 1 Å (compare with Fig. 3.3) one gets as an upper limit

$$\tau_{CC} \approx 0.142 \text{ fs}. \quad (4.2.6)$$

Since bond formation and breaking are the processes to be resolved a constant time step

$$\Delta t = 0.1 \text{ fs} \quad (4.2.7)$$

is chosen. Further tests in chapter 5.1 will demonstrate the validity of this choice.

4.3 Thermostat & Barostat

In this section tools will be briefly described to control the temperature or pressure of the simulation based on [47]. For the generation of surfaces (see section 5.3) different phases of temperature and pressure control are needed. Due to the conservation properties of the Velocity-Verlet integrator (see 4.1) the number of particles N , the volume V and Energy E is preserved. Therefore, in terms of statistics such a system represents a *micro-canonical ensemble* (NVE ensemble). Sometimes it is desired to keep the temperature constant although the system may gain or lose energy, like during the formation of bonds.

To limit the total kinetic energy of the system a control of the temperature is used, resulting in a *canonical ensemble* (NVT ensemble). This control is implemented by rescaling of the particle velocities. The rescaling factor is calculated from thermodynamic coupling to a *Thermostat* and was derived by Berendsen[48] as:

$$\lambda = \sqrt{1 + \frac{\Delta t}{\tau_T} \left(\frac{T_{ext}}{T_{cur.}} - 1 \right)}. \quad (4.3.1)$$

Here, T_{cur} is the current system temperature computed through eq. (B.1.1), T_{ext} is the desired system temperature, Δt is the integration time step and τ_T is a scaling factor defining the timescale until T_{ext} is obtained.

In the same way Berendsen[48] derived a control factor for the coupling to *pressure bath*, a so called *Barostat*:

$$\mu = \left[1 + \frac{\beta \cdot \Delta t}{\tau_P} (P_{cur} - P_{ext}) \right]^{\frac{1}{3}}. \quad (4.3.2)$$

P_{cur} is the current system pressure computed by (B.1.3) and $P_{ext.}$ is the desired system pressure. Additional Δt is the time step for the integrator, β is the isothermal compressibility of the system. This is the inverse of the *bulk modulus*, which is set in LAMMPS as $\beta = 1/10$. τ_P defines the timescale of pressure rescaling. With the factor μ all system coordinates \vec{r}_i and the system size \vec{l} are rescaled

$$\vec{r}_i(t + \Delta t) = \mu \cdot \vec{r}_i(t) \qquad \vec{l}(t + \Delta t) = \mu \cdot \vec{l}(t). \qquad (4.3.3)$$

General Berendsen advises to use scaling factors which are at least one hundred time greater than the time step. From the chosen time step (4.2.7) this results in

$$\tau_x > 0.01 \text{ ps} \qquad (4.3.4)$$

Actually this was the lower limit chosen for τ_T with the upper limit of $\tau_T = 20 \text{ ps}$. The barostat has a much shorter response time. Therefore, at least $\tau_p = 50 \text{ ps}$ is chosen. These values depend on the current simulation parameters, for more details see chapter 5.

These control algorithms can still produce problems and non-physical results. For the Thermostat a common problem is the so-called *icecube effect*, where the whole system rotates around the center of mass. With the simple form of the kinetic energy calculation (B.1.2) a high temperature is obtained while there is only rigid body dynamics. Improved algorithms like Nosé-Hover thermo- and barostats[49] are existing and sometimes used. The penalty is increased numerical effort.

To be able to study the surface interactions in our system major extensions of the LAMMPS code were necessary. These will be characterized in the following section.

4.4 Allocation and removal of molecules

In this section the implementation of molecule allocation and deletion will be presented. To analyze sticking coefficients for a specific molecule, this molecule is “shot” towards the surface with random orientation and from a random position. “Shooting” means that the molecule is launched with a center-of-mass velocity equal to the desired kinetic energy. The molecule moves towards the surface and one of the four cases from chapter 2.3 will happen (sputtering, reflection, sticking or fragmentation). As some surface reactions may need some time to happen the simulation is continued. The limit of the total time for one event is chosen such that reactions within the numerical limits of MD, namely in terms of run time and number of time steps, are finished. Therefore, a total time of 5 ps is simulated for every molecule.

At the end of each process the final state is analyzed with respect to species and process distribution. Algorithmically, the final state of the molecule is diagnosed and remaining bonds are identified. A specific problem is that counting all particles above a certain level to find reflected, sputtered or backscattered molecules is incorrect. The reason for this is that strong intermolecular forces from 3.4 keep products transiently (for a timescale of about $> 5 \text{ ps}$) at and in the first layers of the surface (see section 5.4 for details). After this time, these are released as well. Therefore, all bonds are analyzed and categorized and a dedicated analyze of the covalent bonds is done identifying those contribution of molecules only transiently bond.

4.4. ALLOCATION AND REMOVAL OF MOLECULES

Two tasks arise:

1. repeated allocation of the molecule
2. diagnostics of the molecular structure.

Repetition can be achieved by multiple execution of the same input script with different seeds initializing the random number sequence. The main task was here the creation of scripts to create videos, analysis and plots and to prevent that older runs were overwritten by new runs. In addition, a direct way to allocate molecules in LAMMPS with the AIREBO-potential had to be implemented.

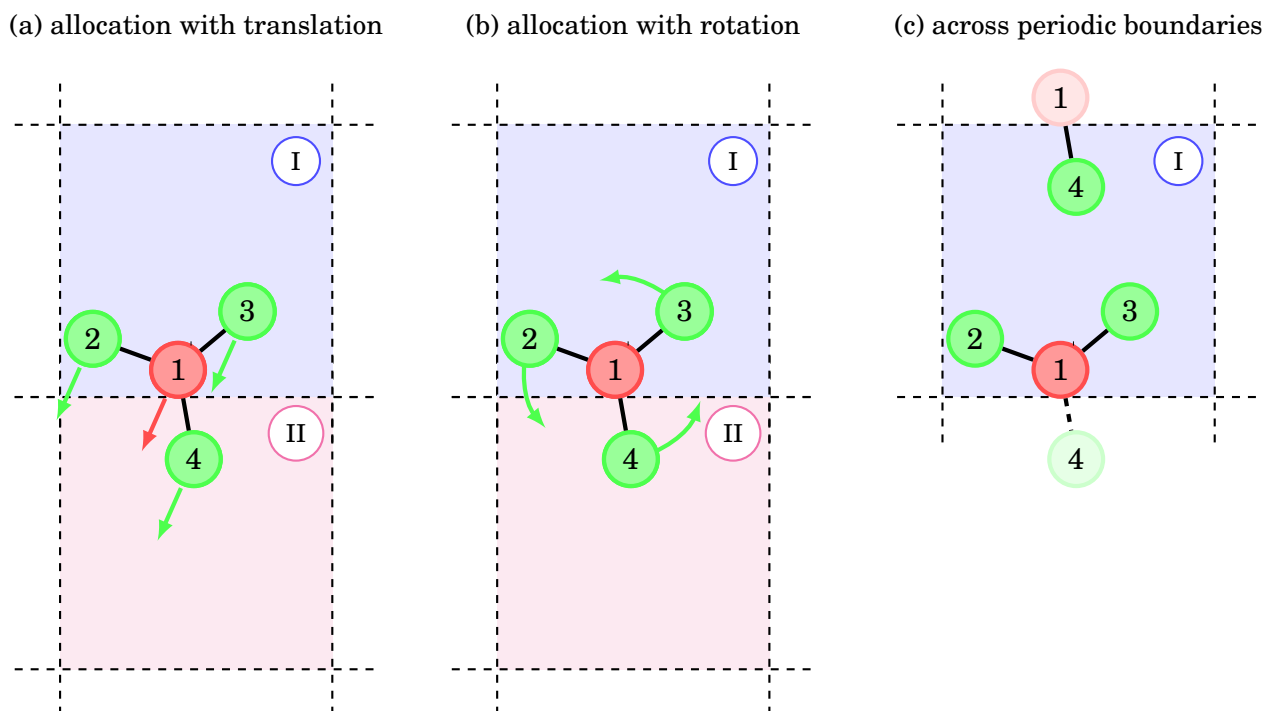


Figure 4.2: Some applications of the implemented molecular source. This can allocate molecules in different domains or across boundaries with translational or rotational energy. Hereby, the energies can be a constant or sampled from a distribution. In 4.2c also the problem to compute bonds across boundaries is illustrated.

Arbitrary molecules can now be loaded from an old LAMMPS-output file (like a simulation of a single molecule) into a C++-class. This class has different functions which allow to rotate the molecule with three arbitrary Euler angles or to add a certain velocity to the center-of-mass or a angular momentum to the whole molecule. These molecules are controlled by a molecular source which is generated from an input-file specifying the frequency, the kinetic and rotational energy and their variance. One molecule can be arbitrarily often included with different parameters through this input-file. Likewise, any energy distribution can be realized.

To allocate a molecule its random position is determined in the master process within the starting region above the surface. Now all processes on the different processors check the topological structure of this point with respect to the chosen parallelization. The check is done via a hard sphere with a center at the center-of-mass and a radius of the most dis-

CHAPTER 4. NUMERICAL IMPLEMENTATION

tant atom excluding possible intersections in all domains. In case there is no intersection conflict detected the different atoms of the molecules are then assigned to these different domains according to the previous analysis. This procedure prevents allocation of an atom near to a surface atom within distances resulting in too large potential energies.

The second task is accomplished via a recursive function. Starting with one atom all its bounded neighbors are assigned the identical molecule number. These neighbors atoms are taken as starting positions, repeating the procedure until all atoms in a domain have a number. One has to prevent endless loops by checking the assignment status. Also ghost atoms end the recursion procedure. Free molecules are identified by excluding bounded ones. For this, every domain checks if a molecule fulfills a deletion criteria like 'atoms of a specific group being bounded in it' or 'no member outside of a specific area'. In case, a molecule can not be deleted directly because it exists across domain boundaries each process checks to which neighbor domains it belongs. Finally, all bonds are identified from a simple threshold distance one can distinguish between intra- and inter-molecular bonds.

The implementation was done in LAMMPS modifying the source code. Due to the new option of a molecular source a box can be filled with different molecules in a pre-defined fraction allowing the creation of a sample surface (see Section 5.3). Also, a continuous bombardment of a surface is much easier because not every individual molecule has to be defined in the input-file.

In this chapter the basics of the simulation tools were presented, necessary for this work. In particular, special adaptations of the source code were described. Now, all tools are at hand to address the central question of this work, namely the analysis of surface interaction in carbon fluorine plasmas.



5

RESULTS

In this chapter results from MD calculations of fluorine carbon systems are discussed. The first task elaborated in section 5.1 is the test of the implementation of the potential through binary collisions. Secondly, surfaces had to be created on which the impacts were performed to calculate sticking coefficients of selected species. The creation of surfaces is outlined in section 5.3 as well as some problems that arise during that process. In the section 5.4 sticking coefficients are computed. The work was done in collaboration with Bandelow, who also made a first analysis of the influence of sticking coefficients in his global model for a CF_4 -plasma. This will be presented in section 5.5.

5.1 Validation of the implemented changes

For the simulation of the fluorine carbon system no potential was available in LAMMPS[44]. Therefore, additional routines for an adequate potential had to be implemented into the source code. Extending the existing AIREBO-potential of LAMMPS from two to three species was necessary. The coefficients for carbon-carbon, carbon-hydrogen and hydrogen-hydrogen interaction were already existing in LAMMPS. The ones for carbon-fluorine and fluorine-fluorine interaction were taken from the open source code of Jang et al. [40]. All Lennard-Jones interactions are also included from there.

After this extension a validation of the implementation of the potential is needed. This is not a validation of the potential itself, because functional forms and parameters were taken as predefined from literature. For this test the same atomization energies of the formed molecules as Jang et al. were used (see Fig. 5.1). While for hydrocarbons the agreement is fairly well for fluorocarbons some differences exist. These differences were resolved and accepted after direct consultation with the Sinnott group.

Tests for bond-lengths and molecular geometries for selected species showed fairly good agreement with one exception. CF_2 is linear when computed with this potential despite

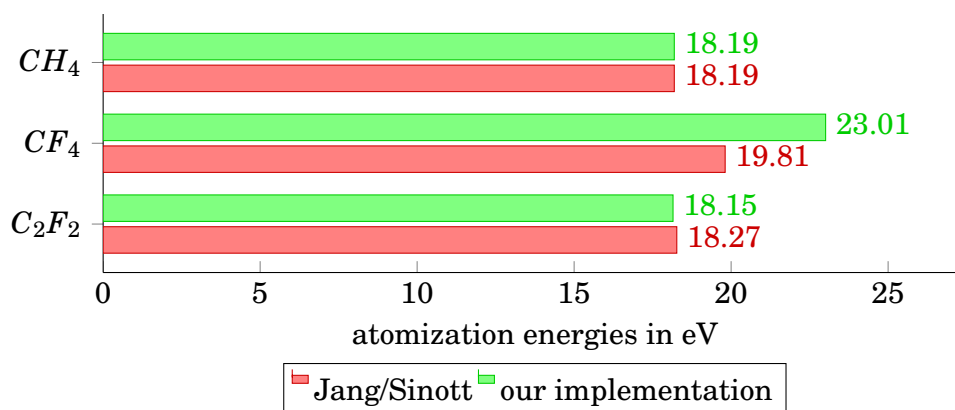


Figure 5.1: Differences in atomization energies. Complete list see Figure B.3.

it is bend in reality.

An additional test that was performed successfully is a translation test. Here, a molecule is moving at a speed of 100 \AA ps^{-1} through the simulation box with periodic boundaries for a long time period. The test is passed if the molecule remains stable and only little energy is transferred into the molecular internal structure. An extension of this is the addition of rotational energy. As molecules like CF_4 are stable with kinetic and/or rotational energy larger than their atomization energy, this test succeeded.

Additional testing of the implementation is done by direct probing of the potential and binary collisions. Direct probing means, that atoms were inserted at certain positions and the calculated potential was compared to the expected one. The agreement is quite satisfying.

Binary collisions do not only test the implementation but also the momentum and energy conservation. Their analysis revealed with a violation of the momentum conservation an implementation error in the Lennard-Jones part of the potential. In the diagnostics of the collision dynamics the implemented potential is also checked. Comparing the detected potential with the expected one allows its validation, similar to direct probing. Figure 5.2 shows a collision of two carbon atoms.

As the potential energy and the distance are both shown as a function of time the potential can be calculated. Transferring the temporal dependence into spatial coordinates a comparison was done with the original potential of figure 3.3 and gave excellent agreement. While Figure 5.2 seems fairly symmetric, energy and momentum conservation is not perfectly fulfilled. This error is reduced by a smaller time step. However, it remains and a modified algorithm is tested to improve the situation.

Figure 5.3 shows the total system energy as a function of the distance between the two carbon atoms. The red line indicates the energy during the approach of both particles and the green line while they depart. The total energy is not constant but slowly varying. A clear discontinuity at the start of the cut-off region shows up. The variation of the total energy in the unperturbed interaction region follows roughly the potential multiplied with its second derivative. As the Verlet-algorithm is only accurate up to second order this variation is a normal integration error. The jump at the start of the cut-off region indicates a problem with a switching function.

Indeed, the switch (3.2.4) is non-continuous in the second derivative. Therefore, a change

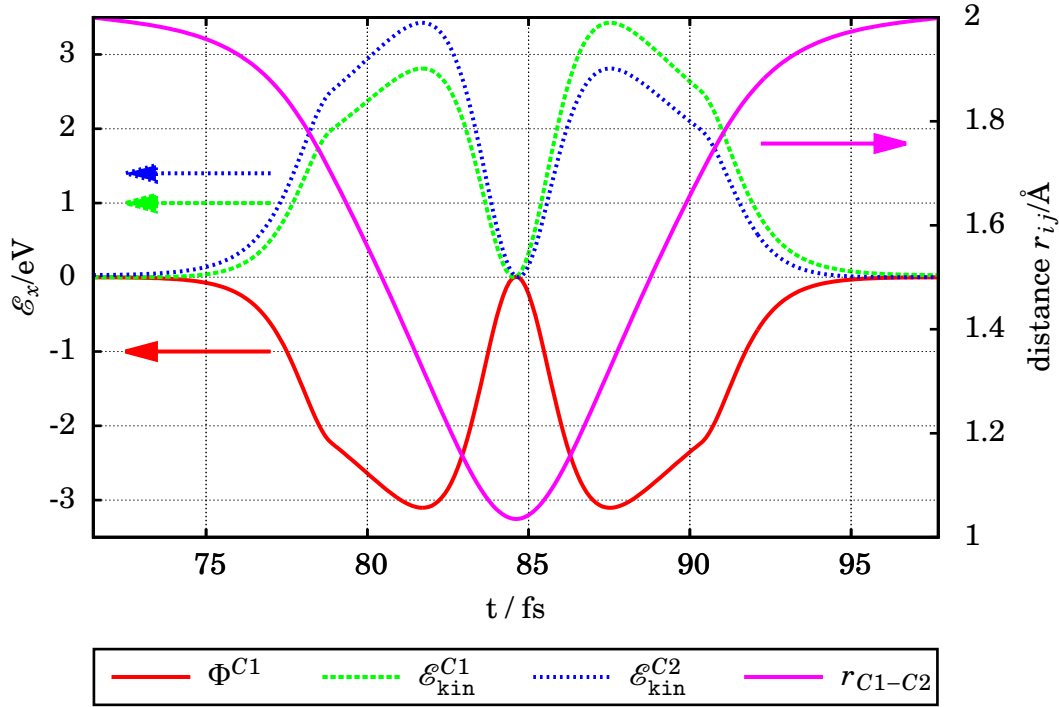


Figure 5.2: Development of the potential and the kinetic energy during a collision of two carbon atoms.

of the switching function was performed. This results in the blue line showing the same oscillation during approach and departure of the two carbon atoms. This way the problem at the start of the cut-off region is relaxed. Nevertheless, further deviation still remains. Artificial numerical heating is a serious problem, which will be investigated further in the following.

5.2 Numerical heating and switch modifications

Numerical heating is an effect of summed integration errors and can therefore not be avoided. In time these errors destroy the conservation properties. Frequently, they result in a gain in temperature, called *numerical heating*. As the integration errors should get smaller with a smaller time step they can also be a limiting factor for the time step. The evolution of the total system energy as a function of time was investigated for a surface in the absence of any barostat or thermostat, which would add or extract energy from the system. This is shown in Figure 5.4. The fit using a linear regression reveals a gain in energy of

$$\Delta E \approx 0.14 \text{ eV ps}^{-1}. \quad (5.2.1)$$

Remarkable is here that the numerical heating is independent of the time step. Therefore, it is assumed that this rise is not due to the normal integration errors but is superseded by an implementation error or error in the potential. A possible candidate is the discontinuity in the second derivative of the switch discussed for binary collisions in section 5.1.

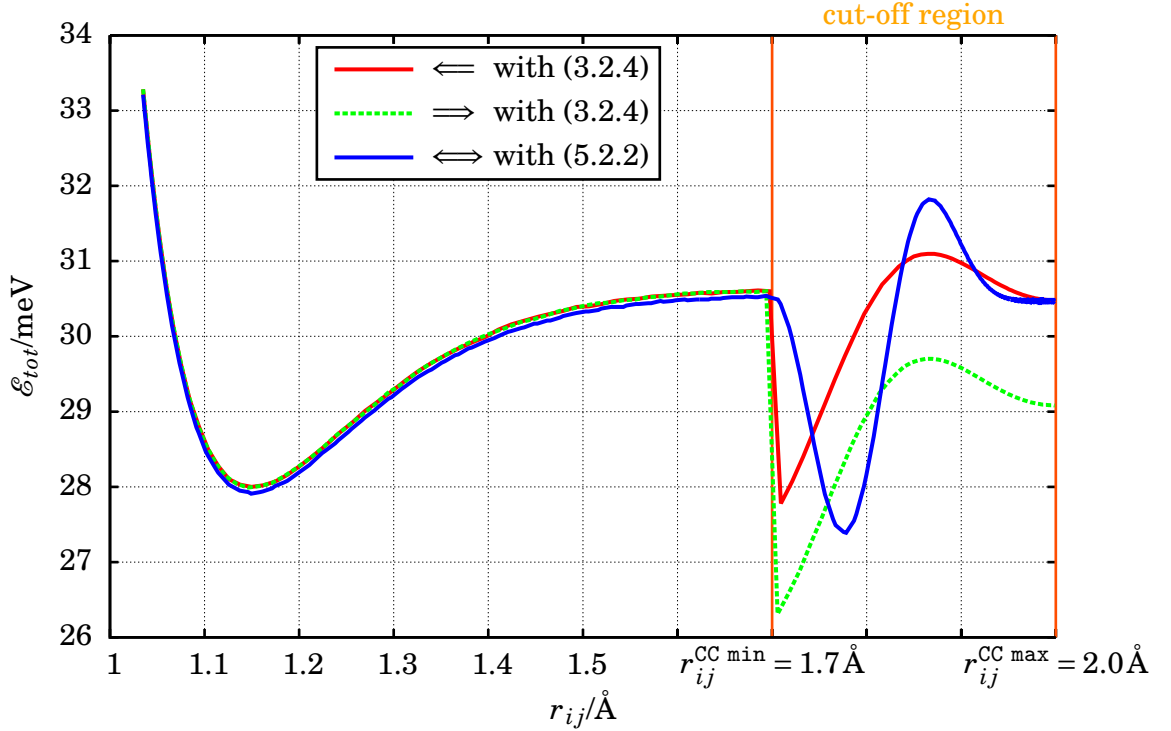


Figure 5.3: Analysis of the evolution of the total system energy in dependence of the different functionals of the switches. The first part follows the trend of the product $\Phi_{ij}(r_{ij}) \cdot \frac{\partial^2 \Phi_{ij}(r_{ij})}{\partial r_{ij}^2}$.

Following the analysis of binary collision in the previous section it was tried to change the switching term from eq. (3.2.4) to a function that is also zero in the second derivative (see Appendix B.1.3). The system of equations for the boundary conditions was solved with Splines, Hermite and Chebyshev polynomials.

The spline interpolation is not continuous in the second derivative and therefore no improvement was obtained. The solution of the Hermite interpolation is satisfying and additional polynomials are computationally cheaper than cosine-functions. Finally, the solution of the Chebyshev interpolation was chosen due to its analytic similarity to the original switching function. Without the Heaviside functions and $t(r_{ij}) = \frac{r_{ij} - r_{ij}^{\min}}{r_{ij}^{\max} - r_{ij}^{\min}}$ follows

$$\tilde{f}_c = \frac{1}{4} \left[2 + \cos(\pi \cdot t(r_{ij})) \cdot \left[3 - \cos^2(\pi \cdot t(r_{ij})) \right] \right]. \quad (5.2.2)$$

As can be seen in Figure 5.4b the new switch (5.2.2) does not reduce the numerical heating, but in fact increases it. The error made with the original switch is a cooling term, which is quite uncommon. On the other hand the new switch is computationally more costly as some more operations have to be made to calculate it. While this seems insignificant at first sight, this function is called up to a million times per time step. Therefore, even one additional operation will have a negative impact.

It must be admitted that the source of the heating could not be identified. Possible sources of the heating are contribution to potential not accessible by the binary collisions tests, like local coordination influence on the bond-order term, or truncation effects

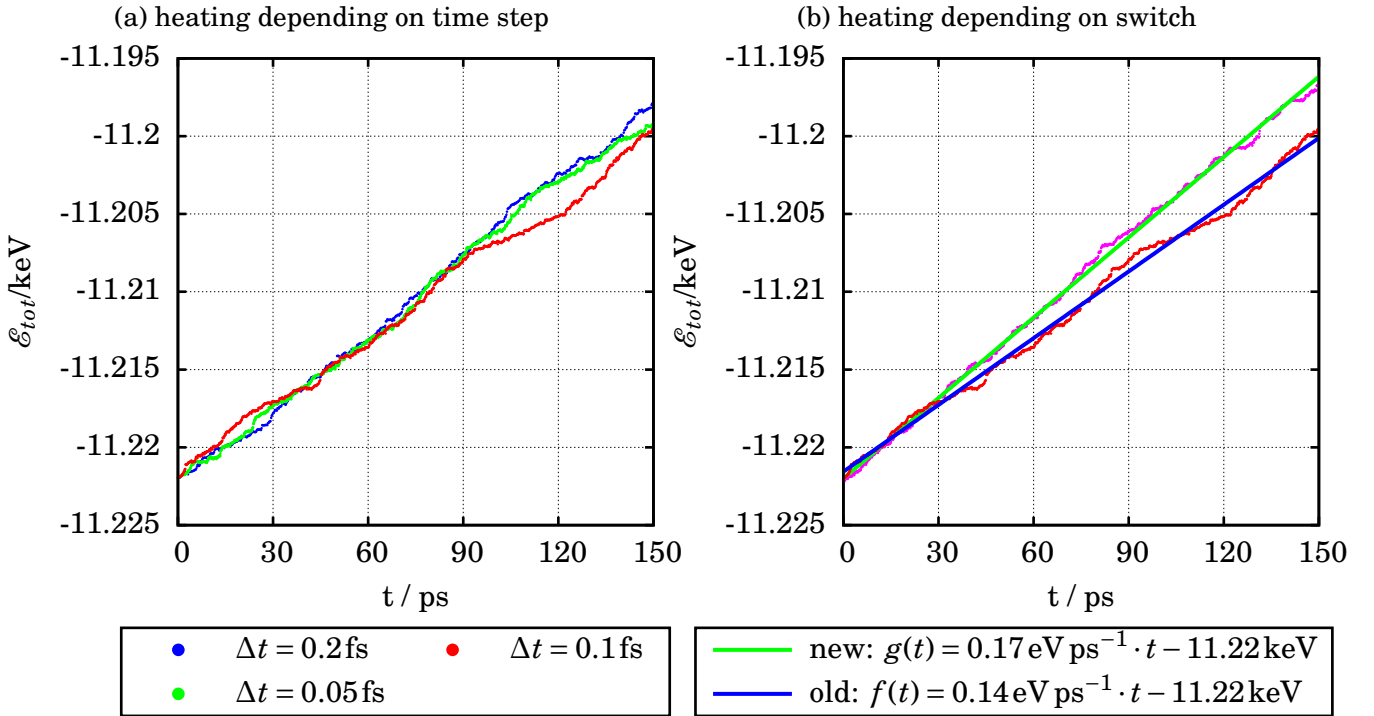


Figure 5.4: Evolution of the total system energy as a function of time for a surface of 2000 particles without any thermostats. The left figure shows the independence of numerical heating from the chosen time step. In the right figure the influence of different switch functions is shown.

of the Lennard-Jones potential.

For the runs to calculate the sticking coefficients numerical heating is not a problem as the net gain in energy per bond ($\leq 0.5 \text{ meV}$) is negligible due to the short simulated times of 5 ps. In addition, these runs have also active thermostats. Further details will be presented in section 5.4.

For other applications numerical heating is quite limiting as it prevents reasonable long simulation runs without a thermostat. Thus, the process of surface generation is performed with at least some regions of the simulation box with barostats and/or thermostats as will be shown in the following section.

5.3 Generation of surfaces

In this section the procedure to create amorphous surfaces with certain properties will be described. Unlike normal solids amorphous films have no ordered crystal structure by which they could be allocated easily. So, they must be prepared numerically in a special procedure. Sizes and bonding characteristics of the ingredients need to be defined. For the system considered in this work both electrodes and reactor walls are of interest. Both have quite different characteristics as presented in section 2.2.

To get the desired density of the sample the simulated surfaces have to consist of

$$N \approx 1800 \text{ atoms} \tag{5.3.1}$$

CHAPTER 5. RESULTS

with chosen dimensions of the simulation box (see section 4)

$$x = 25 \text{ \AA} \quad y = 25 \text{ \AA} \quad z = 35 - 45 \text{ \AA}. \quad (5.3.2)$$

This leads to surfaces with a density of

$$n = 1.6 - 2.2 \text{ g cm}^{-3} \quad (5.3.3)$$

well in agreement with the experiments (see section 2.2). Assuming perfect sticking and a growth rate of $\Delta d = 500 \text{ \AA min}^{-1}$ a CF_2 molecule has to hit the surface every $\Delta t = 7.2464 \text{ ms}$. It is therefore justified to assume a perfectly equilibrated surface for every incoming molecule. This holds even for sticking coefficients larger than 10^{-6} .

For simplification it is assumed that only carbon fluorine films are facing the plasma and no uncovered parts exit of the stainless steel reactor wall. This is justified because due to the low kinetic energy of the incoming particles only deposition occurs. Experimental film heights are typically larger than 100 nm[13].

The procedure for creating surface samples should be automated for different structures. Using multiple samples can minimize the risks to obtain artifacts from a single film. For the production of carbon-fluorine films two different ways were evaluated.

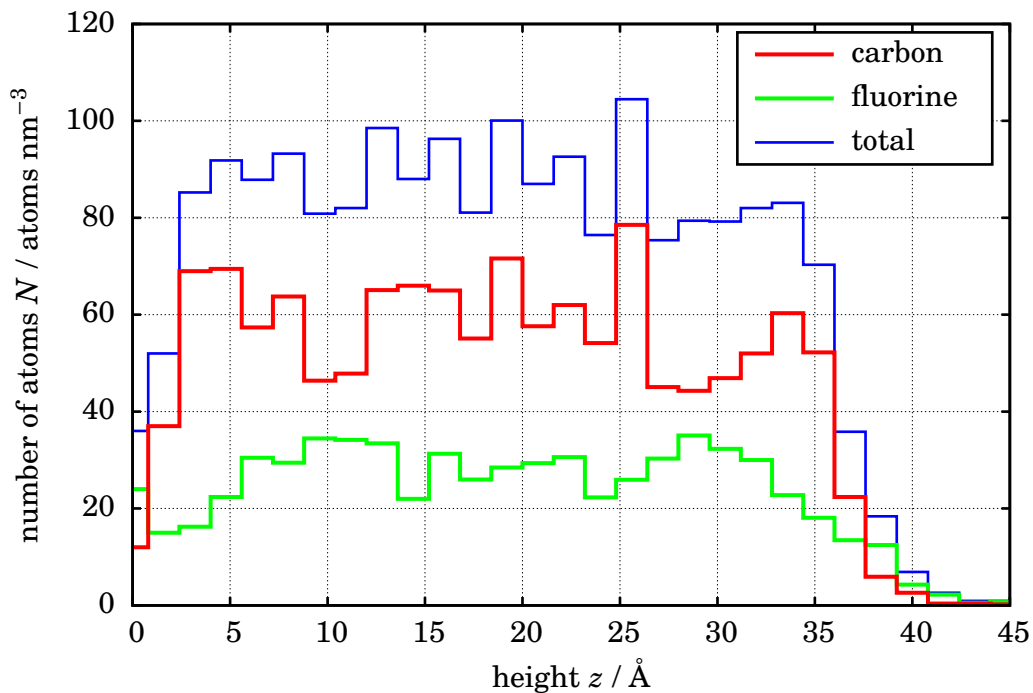


Figure 5.5: Example distribution of fluorine and carbon in a surface

The first is to modify dynamically a solid. Here, a solid with a given structure is bombarded by molecules and the structural changes are followed as a function of time. The main problems, why this method was not chosen, are the lack of sputtering at the energies investigated and the low sticking rates. Both lead to unacceptable small changes resulting in too long run times.

The second approach is to create the surface by random allocation of atoms, radicals or molecules in a volume as described by Sharma[50] and Traeskelin[51]. The formation of

the structure is obtained by an equilibration process described in the following. The main advantages of this procedure are the straightforward composition κ of the surface by the input species and its homogeneity (see Figure 5.5). The creation of the samples are a necessary prerequisite for the computation of the sticking coefficients. The procedure of sample preparation is shown in Figure 5.6. The temporal evolution of height is plotted and the different regimes are indicated by color.

5.3.1 Creation process

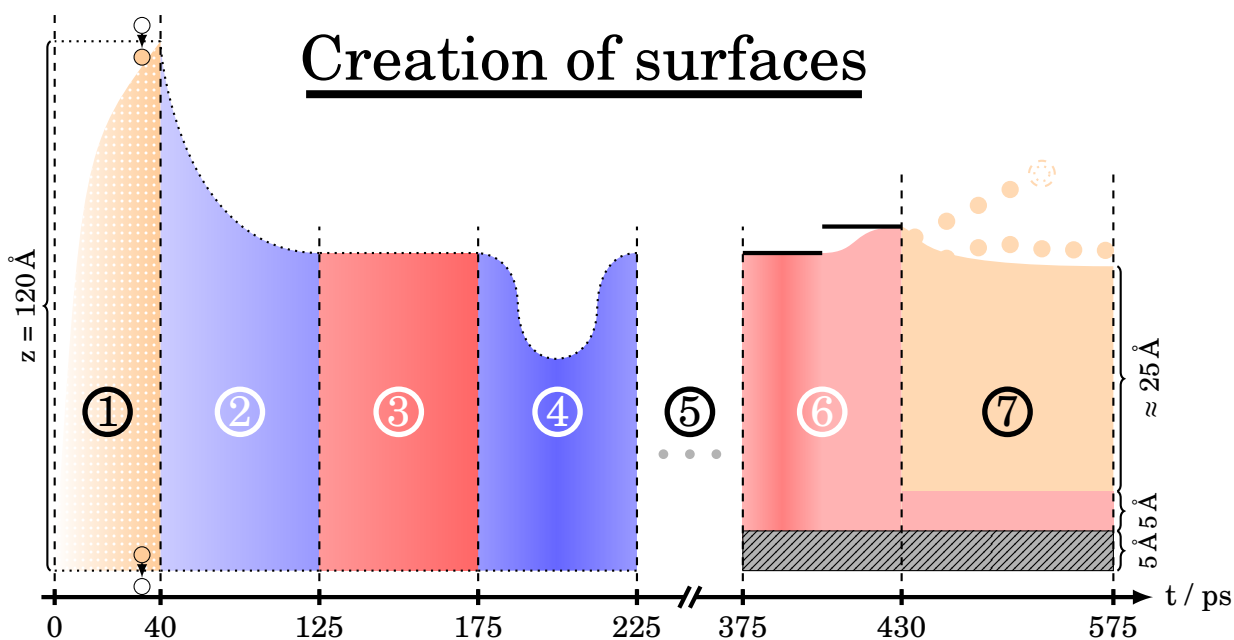


Figure 5.6: The temporal evolution of the simulation-box height. Different ensembles are characterized by their color. Orange symbolizes a period, where the system develops freely. During red periods the velocities are rescaled to reach a desired temperature. During blue periods the volume is changed to adjust the system to a certain pressure. The saturation level of blue or red indicates the strength of the acting barostat or thermostat. The hatched region represents fixed parts of the sample. Dotted lines are periodic boundaries while a thick line represents a reflecting wall.

- ① A periodic box is filled with particles at random positions. These are atomic fluorine and carbon in the desired fraction κ . In principle, also radicals or big molecules like CF_2 , CF_3 or $\text{C}_{41}\text{F}_{84}$ could be used. Especially for big molecules the simulation box has to be of appropriate size to prevent overlapping of the allocated molecules, which could cause numerical artefacts. During this phase a viscous velocity damping term should be applied, because when bonds are formed huge amounts of energy are transferred from potential to kinetic energies. To avoid too strong energy transfer only single particles are slowly and separately added. This defines the duration of this phase of up to 120 ps.

- ② This phase is only needed if molecules are involved. Allocation of atomic species only usually creates sufficiently dense systems. Simulation boxes filled with big molecules have to be compressed to bring them together.
- ③ During the third phase the whole ensemble is heated up through a thermostat. In case a system should be created with minor modifications of the initial ingredients low temperatures have to be chosen (1000 K to 1500 K). To create completely new structures compared to the initial setup the final temperature has to be much higher (over 4000 K).
- ④ A high pressure barostat is applied. While this is usually used to achieve a certain fraction of sp^2 to sp^3 hybridization these simulations showed only small differences for different pressures. Sometimes, this high pressure phase leads even to a crash of the simulation. Such an event is discussed in detail in section 5.3.2. Attempts during this phase to produce ordered diamond or graphite structures from pure amorphous carbon through high pressure were unsuccessful.
- ⑤ Additional thermostats and barostats are applied. For some surfaces phases ③ and ④ are repeated. In the process of creating a PTFE-like surface in this phase the temperature is lowered to 300 K and through a barostat the surface is guaranteed to be stress-free. Also during this phase the surface is shaped to the desired lengths in x and y of 25 Å.
- ⑥ Up to now periodic boundary conditions were applied in all directions. Now, the periodicity in z is no longer used. Some bonds are cut, therefore the surface is not longer equilibrated. To prevent a direct loss of particles at the top layer a reflecting wall is installed. Atoms in the lowest layers are kept fixed as carrying layers of the whole surface. The depth of these layers is 5 Å. The other atoms are slightly heated to equilibrate the generated defects. In this process the limiting top wall is lifted step-wise upwards.
- ⑦ The reflection wall is now removed completely. A layer of 5 Å above the fixed atoms is controlled with a thermostat. This is necessary to dissipate the energy gain from numerical heating and to prevent the reflection of waves created from impacting molecules. Some of the loose bounded molecules may leave the surface and are then taken out of the simulation. All molecules with no covalent bond outside the top layer of approximately 10 Å are removed, because the pure Lennard-Jones bond is too weak and results in additional losses of molecules from such a surface. This contribution would disturb the analysis of sticking. A criterion for a stable surface is that only a fraction of up to a fourth of all its atoms is lost at the end of this phase after ≥ 150 ps. Then, this phase is extended for a simulation time of up to 300 ps to research “long” time stability.

Simulations to create surfaces using this procedure take on a normal PC with a Quad-Core-CPU around three days. Here, extensive use of the parallization of LAMMPS was made. The resulting samples are discussed in section 5.3.3. Before this, one example is presented, where the surface generation process failed due to numerical problems.

5.3.2 Problems with barostats during equilibration

In this section one example for an unsuccessful surface preparation using a barostat will be presented. To produce a PTFE-like surface with 16 $C_{41}F_{84}$ molecules the simulation fails. During phase ④ an irregular gain in kinetic energy is detected, which crashes the simulation numerically (all values become “Not a Number”). A successful counteraction is to reduce the desired pressure from 1×10^{11} Pa to 8×10^{10} Pa (start pressure is 5×10^{10} Pa and $t_p = 50.0$ ps is chosen).

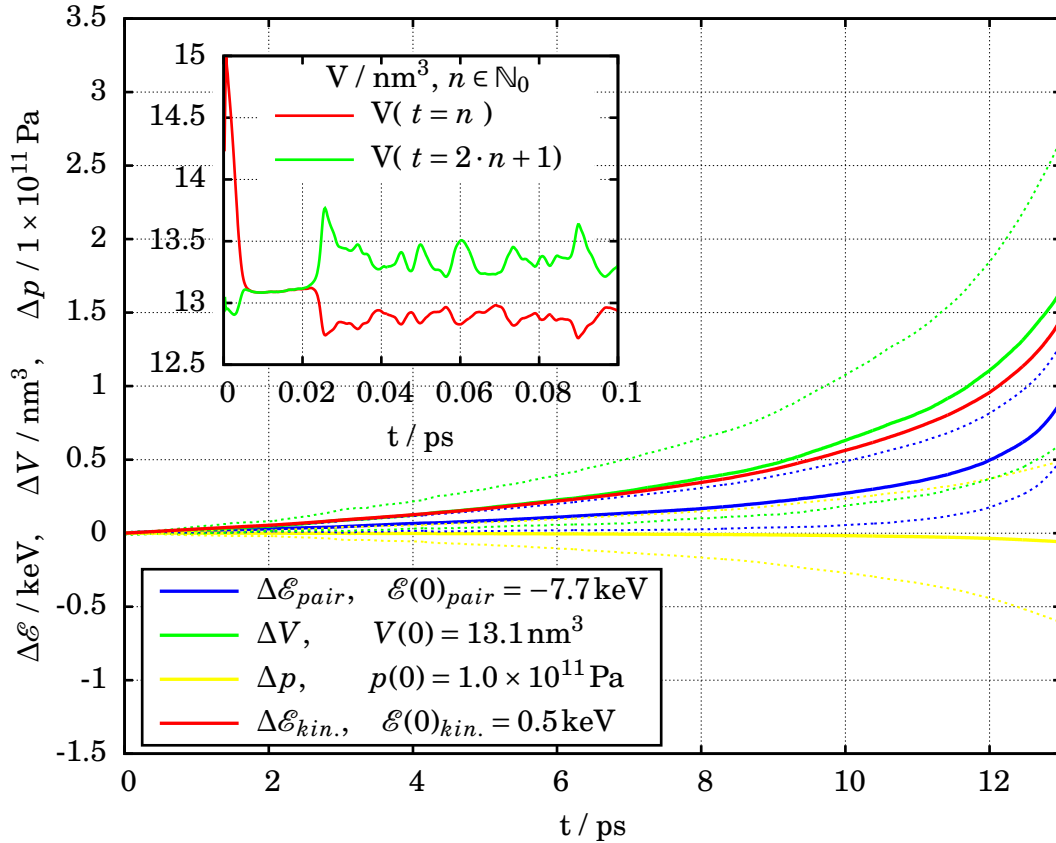


Figure 5.7: To get a harder surface through a barostat a high pressure was applied by modifying its volume. After a short time a bifurcation occurs, leading to heating until the numerical failure of the simulation takes place. In the main plot energies, pressure and volume are plotted as moving average with a window size of $\tau = 5000$.

A detailed analysis reveals an oscillating behavior of the used Berendsen barostat from eq. (4.3.2) (see Figure 5.7). The barostat controls the volume and its effects are shown in the smaller upper graph. At first an oscillation occurs at the start when the volume is scaled to enforce the new pressure. But it is stabilized after a short while. Then, a bifurcation occurs where the volume jumps in size each time step between the red and the green line. Additionally, the volume for the odd and even number of time steps starts to oscillate around their means.

Figure 5.7 shows in large the mean volume as the green line, whereas the dotted green lines are the means of the even and uneven time steps of the volume. As the strong

oscillations of the even and uneven branches would mask all other plots, moving mean averages of 5000 time steps are plotted. The barostat seems to work as intended as the mean pressure approaches the desired value $\mathcal{P} = 1 \times 10^{11}$ Pa. However, due to the rescaling atomic positions are distorted and artificial acceleration of the atoms is created. The result is a constant gain in temperature/kinetic energy. As the velocities are not rescaled through the barostat this parameter is not oscillating. To counteract the temperature gain from the pressure calculation (B.1.3) follows that the volume has to be increased to keep the pressure constant.

The growing volume allows larger corrections by the barostat leading so to a stronger oscillation. The stronger variation of positions causes a larger variance in the potential energy and this way increased acceleration. The effects amplify until the complete failure of the simulation.

The fluctuation of the means are investigated further by fitting a third order polynomial. The analysis through the *auto correlation function* and a *discrete fourier transformation* (DFT) reveals no characteristic frequencies. This analysis is shown in the Appendix in Figures B.4 and B.5.

5.3.3 Results

More than 100 different attempts to create surfaces were made. Only a small fraction were stable. The stability of carbon fluorine films is dominated by the carbon-carbon bonds. Therefore, the more the carbon fraction decreases the less stable are the films.

Additional stabilization is caused by some “big” molecules. These have to be anchored through some atoms in the fixed layer. Then, these big molecules will be the stabilizing skeleton for other molecules. As the mean number of atoms per molecule gets smaller with a higher fluorine fraction, the formation of sufficiently big molecules gets increasingly unlikely. At $\kappa = 1.2$ around 30 % of the surfaces are unstable and at $\kappa = 2$ no stable surface can be produced, if only random allocation of atomic fluorine and carbon is used.

Two examples are shown in Figure 5.8. The upper surface has a fluorine carbon fraction of $\kappa = 0.5$ and was created by random allocation of atomic fluorine and carbon. The input frequency of carbon was double with respect to the one of fluorine. The total computation time was about two days and a half using four cores. The lower surface has a fraction of $\kappa = 2$. It was created by random allocation of 16 $C_{41}F_{84}$ molecules. The removal of the periodic boundaries in z direction cut some molecules in half but basically these molecules are not linked but knotted. The surface holds together through the Lennard-Jones part of the potential and is rather unstable. The creation of such a surface via the polymerization of C_2F_4 molecule or CF_2 could not be achieved.

The upper surface contains 1322 carbon and 650 fluorine atoms. The carbon atoms have 79 % sp^2 and 10 % sp^3 hybridization. Analyzing all surfaces produced with the same fraction ones gets $\bar{f}_{sp^2} = 0.787(7)$ and $\bar{f}_{sp^3} = 0.110(7)$. A larger $\kappa = 1.2$ leads only to small changes of $\bar{f}_{sp^2} = 0.74(2)$ and $\bar{f}_{sp^3} = 0.180(7)$. An example for such surfaces is shown in the appendix (see Fig. B.6).

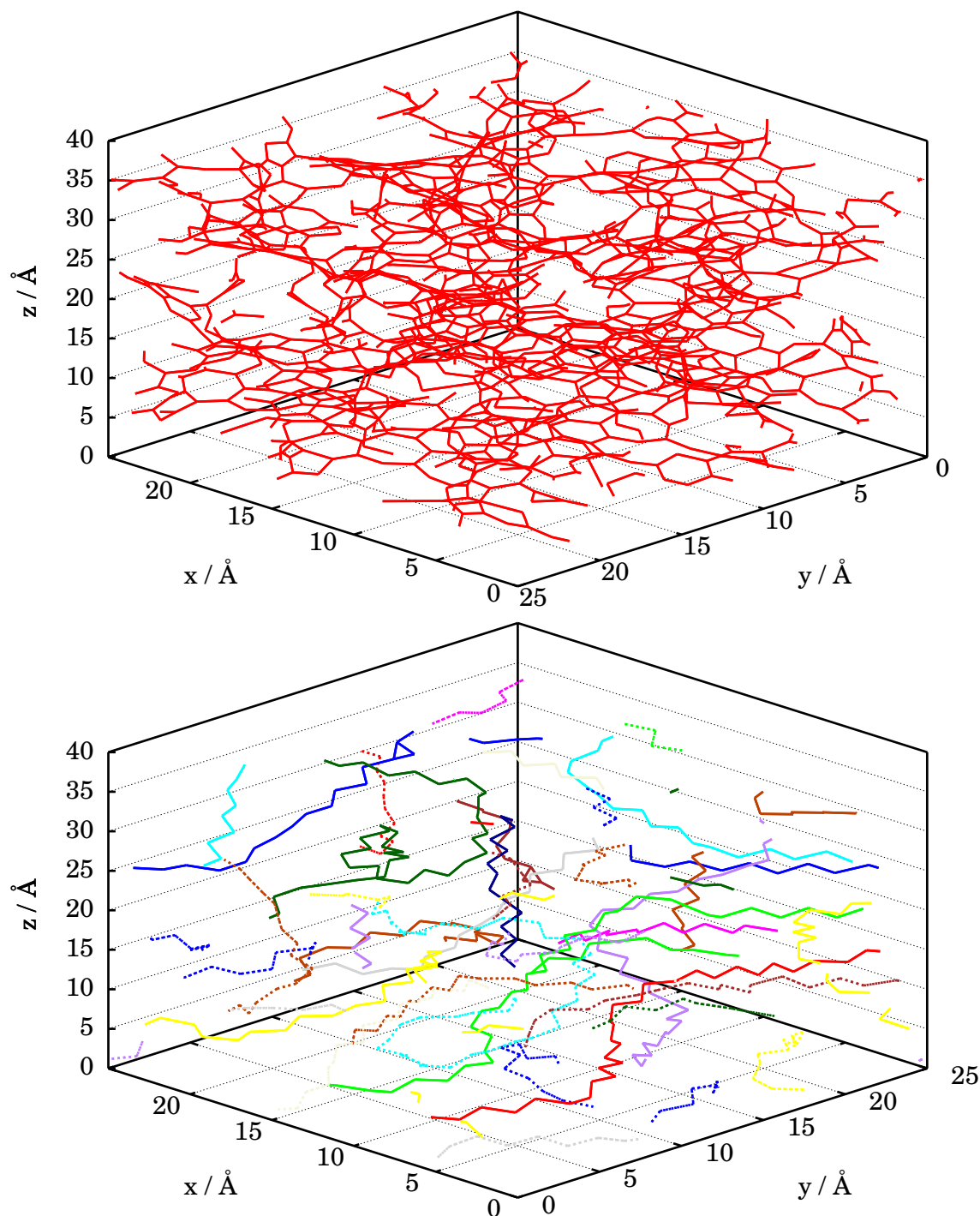


Figure 5.8: Two generated surfaces. The upper one has a fluorine carbon fraction of $\kappa = 0.5$, while the one below has a fraction of $\kappa = 2$. Plotted are only the carbon-carbon bonds. The colors indicate different molecules.

A variation of the pressure applied in phase ③ could not alter the hybridization state of the produced surface. This is a major short coming, because for hydrocarbon radicals a higher sticking is reported for a higher sp^2 fraction[52]. The reason for the lack of altering of the hybridization by the barostat may be the neglect of the torsional term in the AIREBO-potential, which is reported to influence the hybridization strongly[53, 54].

Other reports are that no significant sp^3 fraction for the carbon atoms can be achieved with the REBO-potential for densities below 2.5 g cm^{-3} [55].

The lower surface contained 575 carbon atoms and 1177 fluorine atoms. For these carbon atoms 93% are identified as sp^3 . Due to the unstable Lennard-Jones bonding characteristics of surfaces with $\kappa > 1$ these are difficult to diagnose in terms of sticking, because molecules can just leave the surface due to thermal effects independent of the impacting molecule. At higher energies the loss of surface molecules will be significant. Many of the surfaces with $\kappa = 1.2$ were losing slowly atoms during the long time stabilization after ⑦. Surprisingly, when the thermostat at the bottom above the fixed layer was removed, no such losses occurred. Therefore, it is likely that this thermostat introduces energy although their desired temperature is lower than or equal to the mean temperature of the whole surface. The long time equilibration took around twenty-two hours on four nodes to simulate a time of 200 ps. Carbon-rich surfaces with $\kappa = 0.5$ were chosen for sticking analysis, because of their higher stability. They represent typical experimental conditions at deposited electrode films. Results for sticking coefficients will be discussed in the following section.

5.4 Results of sticking calculations

5.4.1 Discussion of parameters

After creation of surfaces impacts of different molecules were performed to calculate the sticking coefficients. Due to the low number of runs and surfaces no statistical relevant predictions of reaction rates can be made. The analysis is restricted to sticking coefficients as a function of impact energy and surface temperature. The latter dependence was only studied for one species (CF) due to run-time limits.

An investigation of sticking coefficients as a function of the angle between surface and velocity is not necessary because the system is dominated by micro-roughness. The samples are far from single crystals and their surfaces are completely perturbed. Therefore, having a random distribution of starting points is equivalent to sampling the impact angle. Anyway, the local definition of the impact angle is difficult for such non-ideal, amorphous structures.

In the following the sticking coefficients for cold CF_2 , F, CF, CF_3 and CF_4 will be presented for the molecules without internal energy. These molecules were chosen from the analysis of the integrated 0-D model (see section 5.5). Due to the lack of experimental data no further preparation analysis of the initial state is done, like vibrational states. After a molecule impinges onto a surface other degrees of freedom will be excited. The kinetic impact energy is varied between $E = 0.03 \text{ eV}$ and $E = 10 \text{ eV}$. This is only translation energy, following the example of Sharma[50]. The chosen simulated time is 5 ps, which is enough to finish possible surface reactions[56]. In contrast to all other species CF_2 interaction was analyzed only for one surface, because no other systems were available at that time. Later run-time restrictions made it impossible to add further data points.

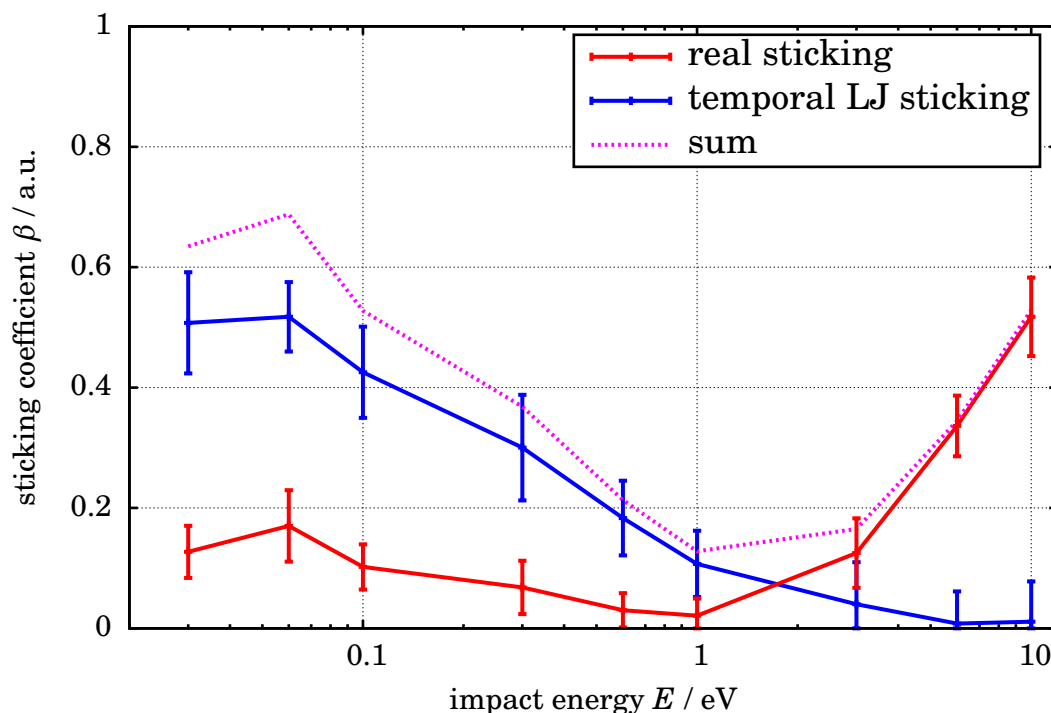


Figure 5.9: Energy dependent sticking coefficient for CF_2 . For low energies a significant part of impinging molecules stays at the surface without forming a bond.

5.4.2 Sticking coefficients for CF_2

The runs for CF_2 are performed on a single surface with $\kappa = 0.5$ and a temperature of ≈ 300 K. If the incoming molecule does not form a covalent bond to the surface, it reveals only *temporal sticking* due to the Lennard-Jones part of the potential from eq. (3.4.2). For timescales larger than the chosen analysis time of 5 ps these molecules will leave the surface. To minimize the run-time the bonding was identified and the Lennard-Jones contributions diagnosed and separated.

The “real” sticking is the contribution from covalent bonds. They are shown as red line in figure 5.9, while the sticking coefficients from temporal Lennard-Jones bonds are shown as blue line. The temporal sticking is large at low energies, because the Lennard-Jones bonds are so weak. At energies much larger than Lennard-Jones bonds the incoming molecule is reflected. Covalent bonds have much larger energies and therefore the probability for sticking increases with energy. The “real” sticking through covalent bonds is small for low energies and rises sharply for energies greater than 1 eV indicating the activation energies for such bonds. The data for low impact energies have large error bars. The decline in sticking may be caused by systematic errors made in the analysis in the region from 0.3 eV to 1 eV.

The general trend of an increasing sticking coefficient for higher impact energies is even to simulation studies performed for hydrocarbons[50, 57]. For them also many reflections occur at low energies. Some experiments report for fluorine carbon films a sticking of $\beta_{\text{CF}_2} = 0.01 - 0.26$ [8, 12, 28] which is in good agreement, if low impact energies are assumed. Otherwise there are also experiments reporting practical no sticking[58, 59].

CHAPTER 5. RESULTS

The experiments show also a large dependency on the surface[59], why more surface should be investigated.

The identification of covalent and Lennard-Jones sticking is done by using as a criterion the distances $r_{max}^{cov} = 2.0 \text{ \AA}$ and $r_{max}^{LJ} = 3.5 \text{ \AA}$. Two systematic errors are possible: the region where the bonds are computed only reaches *to* the surface not *into* it. The border is not computed dynamically so molecules leaving the region by moving into the surface are counted as bounded, despite the lack of any covalent bonding. The Lennard-Jones interaction has a cut-off in its potential minimum. Therefore, the Lennard-Jones sticking is stronger than diagnosed. To avoid both errors the diagnostics area is extended into the surface and the cut-off distance is increased to $r_{max}^{LJ} = 5 \text{ \AA}$.

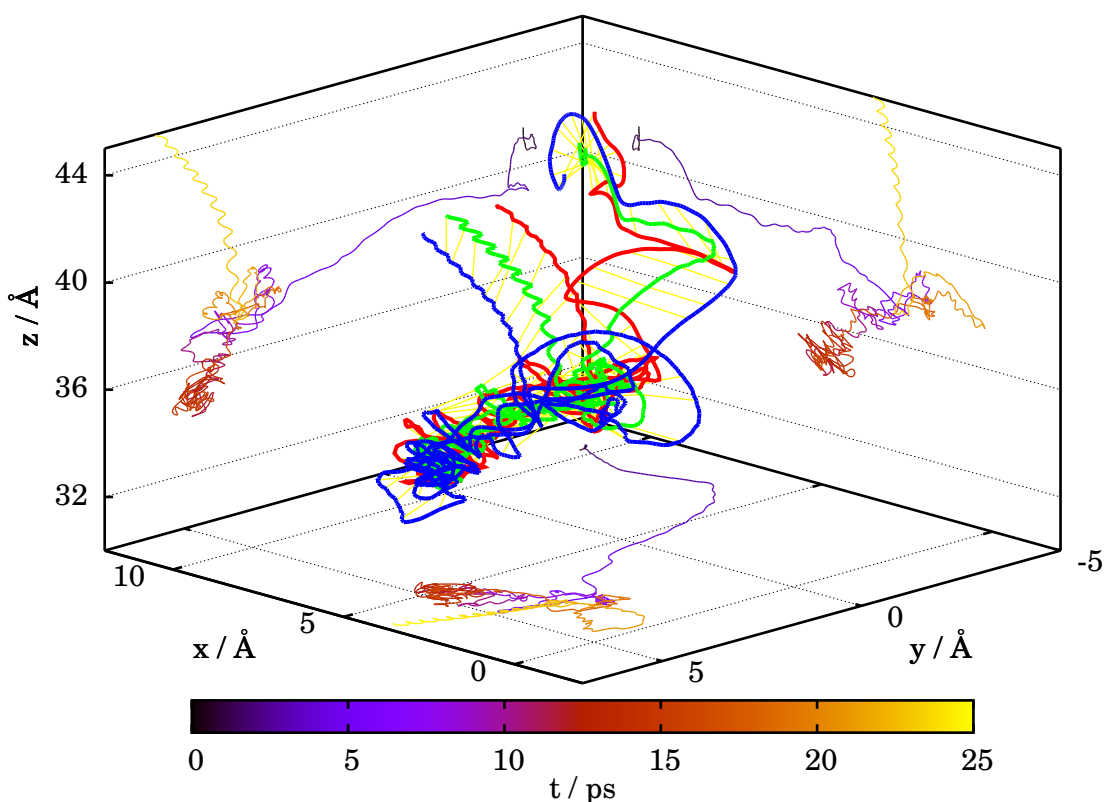


Figure 5.10: One example of temporal Lennard-Jones sticking for a CF₂ molecule. The surface is approximately located at $z \approx 36 \text{ \AA}$. The movement of the central carbon (green) is projected onto sides of the cube. The fluorine atoms are shown in red and blue, while the C-F-bonds are indicated in yellow. The molecule hits the surface, does not form any covalent bond and continues its movement over the surface for about 10 ps. At 10 ps the molecule enters the surface from which it is expelled 10 ps later.

5.4. RESULTS OF STICKING CALCULATIONS

For each energy 999 runs were performed. As error bars the standard deviation is used. Further systematic errors could be introduced through the sampling procedure. For all energies the same 999 impact positions are used. If positions with high or low probabilities for sticking are part of the sample, a bias of the estimate can be introduced due to the small sample size of 999.

Due to the small number (≤ 6) of observed surface reactions (with the surface S)



these can not be quantified in terms of reaction probabilities.

For ten molecules detailed analysis of trajectories was done at an impact energy of $E = 0.03\text{eV}$. One example for such a path is given in figure 5.10. The kinetic energy of the molecule is reduced during the approach. Then it flies along the surface bounded by the Lennard-Jones interaction until it reaches a hole in the surface. After entering the surface the molecule gains some energy due to collisions with surface atoms and is ejected leaving the system. This dynamics happens on a much longer time scale than the simulated time of 5 ps. Therefore, this diffusive dominated process is beyond the limit of this simulation (see section 2.3) and the identification of this contribution is done by bond analysis of the sample. Although several CF_2 were on the surface at the same time, no reactions like the formation of C_2F_4 took place.

CF_2 is in particular difficult to treat because the implemented potential delivers the wrong geometry. This may cause additional errors. It is linear in the simulation in contrast to its tilted geometry. Fortunately, for the other species studied in the following, this problem is not existing.

5.4.3 Sticking results for atomic fluorine

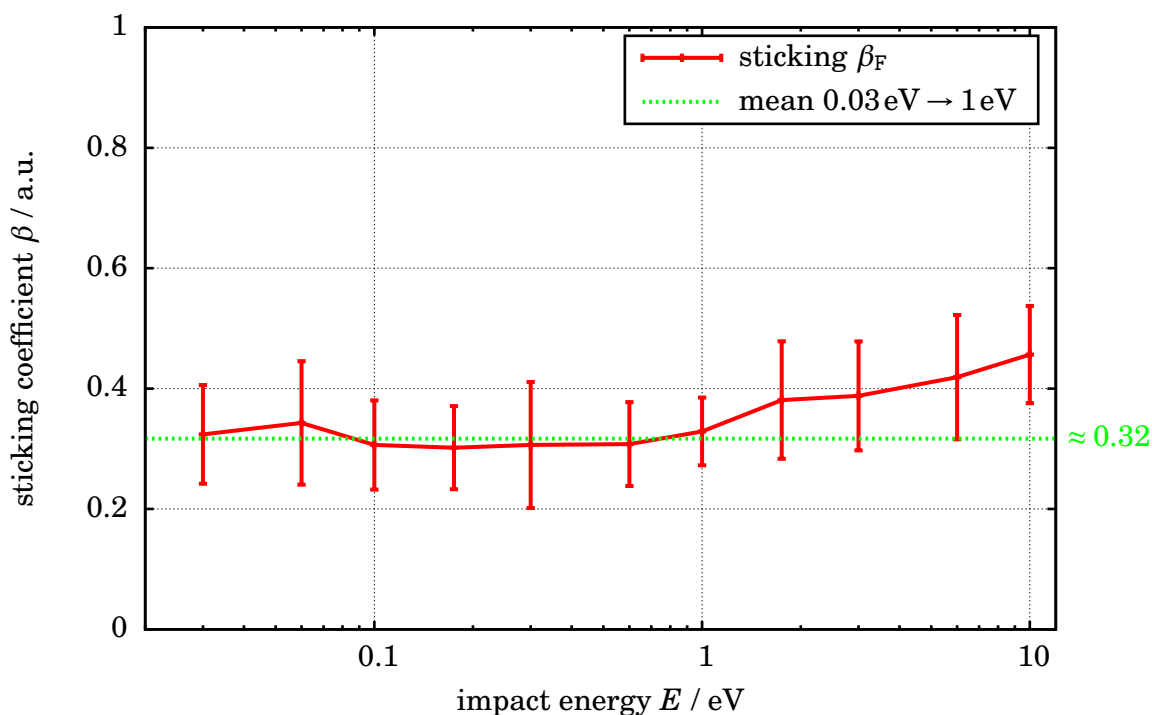


Figure 5.11: Energy dependent sticking coefficient for atomic F. A surface with a lot of carbon was used. The existence of a large number of dangling bonds results in an energy independent sticking. The error bars are the standard deviation of ten different surfaces with $\kappa \approx 0.5$ and no temperature control ($T = 300 - 550$ K).

Here, sticking coefficients for atomic fluorine are calculated from analysis runs on ten different surfaces (see Figure 5.11). Only covalent contributions are shown. Again, for each energy 999 runs are performed. These surfaces are not equilibrated to a certain temperature and have a mean temperature $\bar{T} = 428(64)$ K. They create varying sticking behavior. This results in large standard deviation and large error bars. Due to the existence of a large number of dangling bonds there is a constant sticking probability of $p \approx 0.32$ where no activation energy is needed to form the bond. For energies larger than 1 eV the sticking increases slightly like in the case of CF_2 . Zhang et al.[60] use in their model a sticking coefficient of $\beta_{\text{F}} = 0.3$ for atomic fluorine on polymer layers which is in good agreement with the current result.

Out of these ten surfaces four are releasing weakly bounded molecules. The first one with a probability of $p = 27(9)\%$ is a CF_3 molecule. The process is shown in figure 5.12, but is even more complex than seen in the figure. It is an indirect process: the CF_3 molecule located vertically above the one indicated by the blue circle is expelled and the one in the circle takes its place. Three other surfaces also loose other molecules (see appendix table B.3).

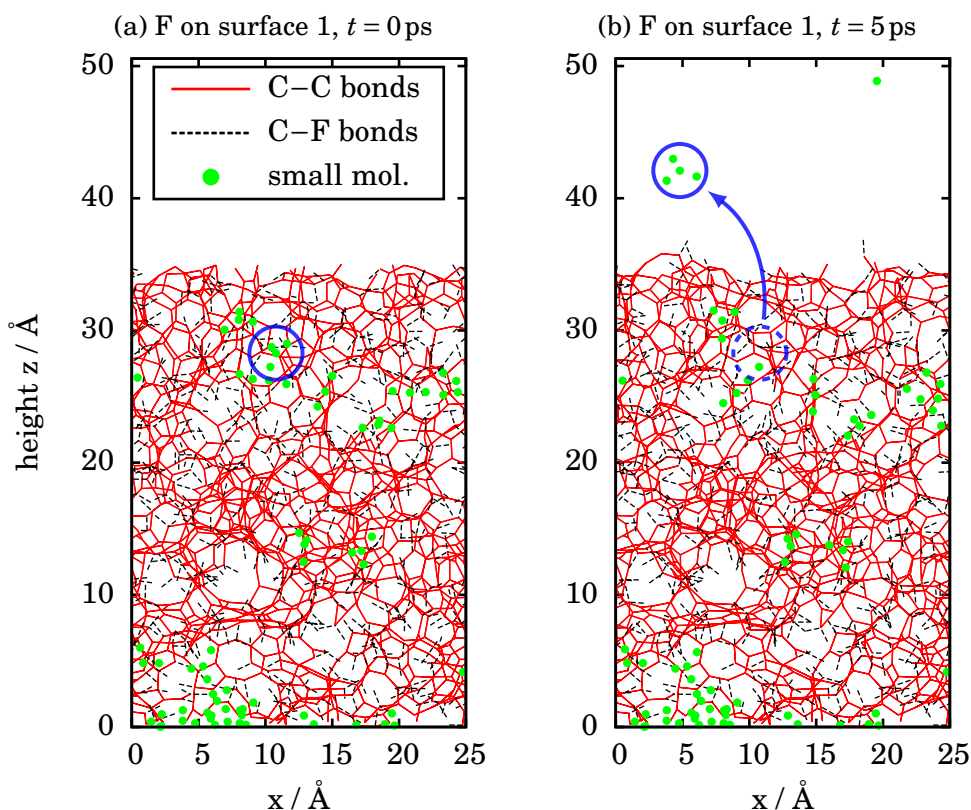


Figure 5.12: Loss of a bulk CF_3 during the impact of an atomic fluorine with $E = 0.03\text{eV}$. In the same region a second molecule is located which is not lost. The loss probability of one CF_3 is $\approx 40\%$ and is decreasing with higher impact energy.

5.4.4 Sticking coefficients for CF

The sticking coefficients for CF are plotted in Figure 5.13 in dependence of impact energy and temperature. Although the number of runs varies strongly between different energies and temperatures (between 300 and 2400), the covalent sticking for 300 K and 450 K coincides. Further, the characteristics of CF are the same as for atomic fluorine but shifted. While for F the energy independent sticking probability is at $\beta_g = 0.32$, for CF it is $\beta_g = 0.16$ (see Figure 5.15). The surface temperature does not affect the covalent sticking but reduces the temporal Lennard-Jones sticking at low energies. Due to the higher temperature more thermal energy is existing for the atoms resulting in larger probabilities to release atoms out of Lennard-Jones bonds.

The computed sticking coefficients are similar to the one measured in experiments ($\beta_{\text{CF}} = 0.02 - 0.15$ [61], lower limit $\beta_{\text{CF}} = 0.14$ and $\kappa = 0.5 \rightarrow \beta_{\text{CF}} \approx 0.4$ [59]). Booth et al. [12] report after the deactivation of the power source a constant sticking of $\beta \approx 0.2$ for both CF and CF_2 . The energy independent sticking for CF and F shows no temperature dependency. This gives further support of the previous results without explicit control of the surface temperature (although their temperature is not higher than 550 K). The temperature dependence seen by Stepanov et al.[61] in their experiment could not be reproduced. The measured effect may be influenced by the changed reactor geometry[7] or diffusive

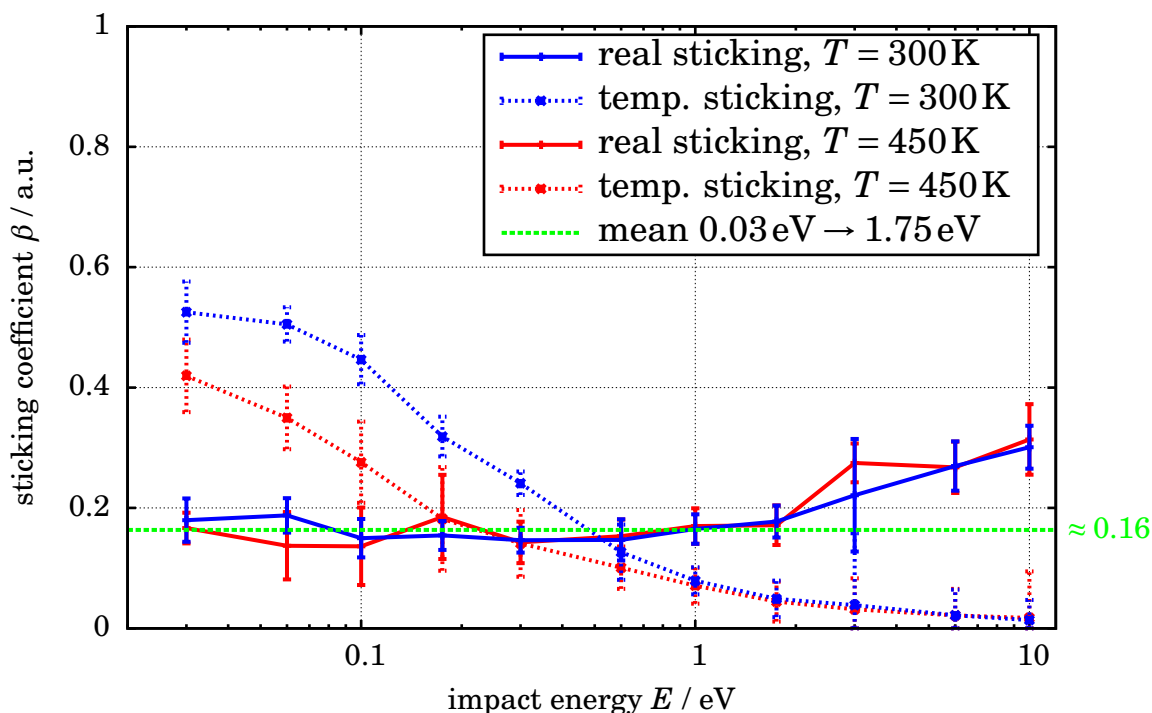


Figure 5.13: Sticking coefficients for CF in dependence of energies and surface temperature. The trend of the covalent sticking is similar to atomic fluorine. The surface temperature affects only the temporal LJ sticking.

processes beyond the scope of this simulation.

In addition, the following reactions are observed with too low numbers (≤ 4) to make a statistical relevant analysis of reaction rates:



5.4.5 Sticking coefficients for CF_3 and CF_4

For the computation of sticking coefficients of CF_3 and CF_4 the same ten surfaces as for atomic fluorine are used. While the characteristics of the temporal Lennard-Jones sticking is the same as before for both species, the covalent sticking is completely different. For CF_3 and CF_4 the sticking coefficients are very small and remain at low level for higher energies.

This low sticking is excepted for CF_4 , because the molecule is non-reactive and needs to be fragmented first for forming bonds to the surface. As discussed below the number of cases with fragmentation remains very low even at 10 eV. This is likely an effect of the implemented potential for which the difference in atomization energies between CF_3 and CF_4 is $\Delta\mathcal{E} = 9.2\text{eV}$ (see Figure B.3). Therefore, removing one fluorine atom from CF_4 requires a large amount of energy and makes it highly improbable that CF_4 is fragmenting.

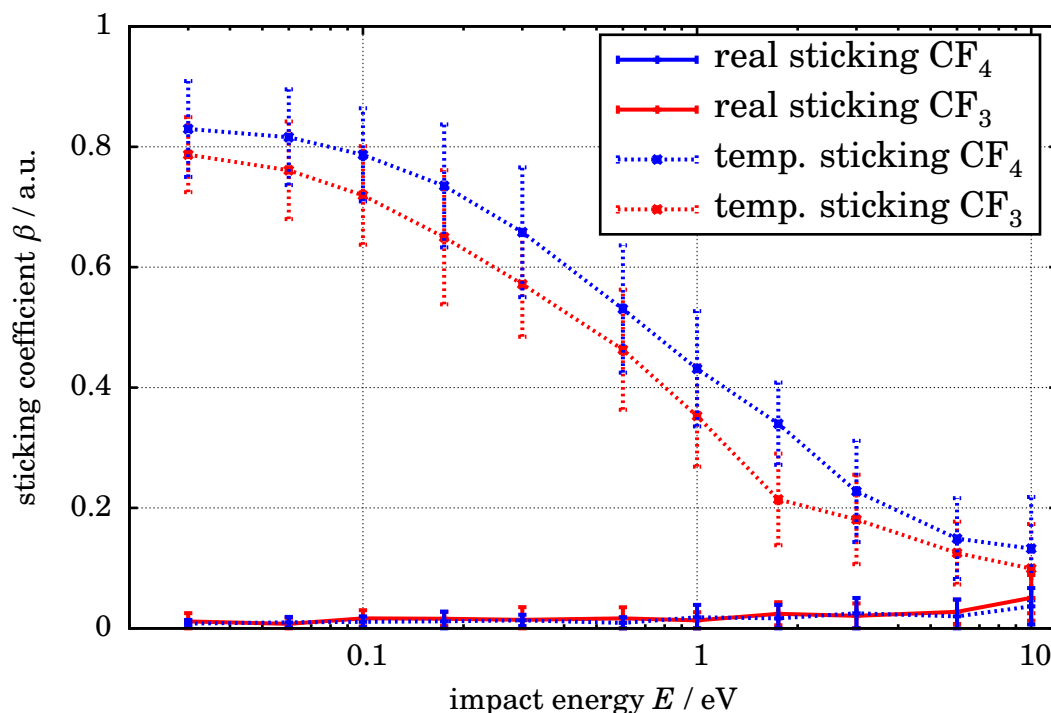


Figure 5.14: Covalent and temporal sticking for CF_3 and CF_4 . The covalent sticking is quite small. In contrast to CF_2 and F the rise at higher energies is only marginal. The temporal sticking shows the same characteristics as for the other species.

The lack of sticking for CF_3 compared to CF_2 is quite unexpected but in line with experiment which reports a sticking coefficient below $\beta_{\text{CF}_3} = 2 \times 10^{-3}$ [59]. Although it is a reactive radical or ion, the reactive central carbon atom is shielded by its surrounding fluorine atoms. After its impact the following species are observed above the surface: (1,2)C, (1-4)F, C_2 , CF, (1,2) CF_2 , CF_3 , C_2F_3 and C_2F_4 . With these species a total sum of 20 different reaction channels are observed. Due to the low number of events ≤ 11 again no statistical relevant predictions can be made. One can distinguish between fragmentation of the incoming molecule and sputtering of the surface. Through sputtering all the listed species are generated. Example reactions for fragmentation are:



None of these fragments leave the temporal Lennard-Jones bonding within the 5 ps simulated. Notable is the lack of CF_4 generated from CF_3 . This may be caused by the low fraction of fluorine in the used surface or simply bad luck due to the low number of runs. The situation for CF_4 is very similar. In total 25 reaction channels are observed with (1,2)C, (1-5)F, C_2 , CF, CF_2 , C_2F_2 , (1,2) CF_3 . As the sticking is lower than for CF_3 one reaction channel



with a probability of 1.1(6)% is found. This reaction happens on all surfaces. Nonetheless, this result should be treated with caution and should be investigated further with

additional surfaces and more runs to get better statistics.

5.5 Sensitivity of the global model to sticking coefficients

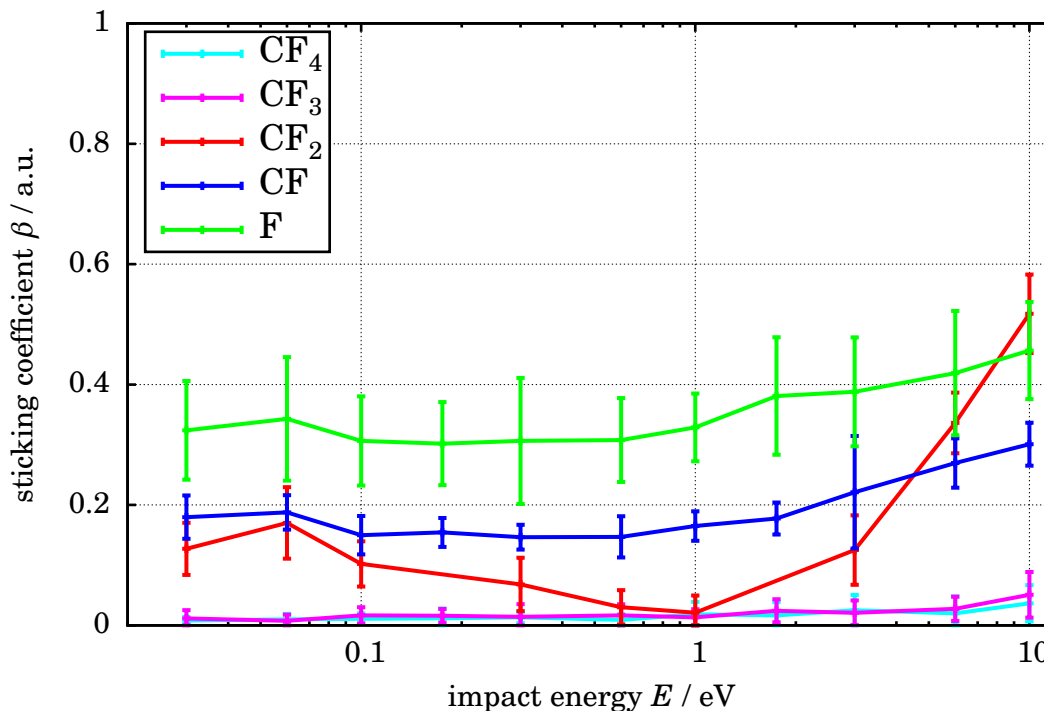


Figure 5.15: The sticking coefficients for all investigated species.

All the computed sticking coefficients are summarized in Figure 5.15. The trend of CF_2 is quite different compared to the other species. Maybe this difference is caused by the missing statistics due to the use of one single surface.

To improve the plasma wall interaction in the global model of Bandelow the calculated sticking coefficients are used. The result is shown in Figure 5.16. Both the contribution from electrodes and reactor walls are presented. The red bins are a reference case filled with CF_4 as feedgas without consideration of any surface interaction (all sticking coefficients are set to zero).

The green bins are results for the case when only reactor walls are considered. Here, the sticking coefficients for an impact energy of 0.03 eV are taken for the computed species. For CF_4 a sticking coefficient of zero has to be used, because even sticking coefficients below 1% lead to numerical divergence and no stable solution. The sticking coefficients of all other species are taken as zero, despite C which is computed with the same sticking as atomic fluorine. Because the ions are confined in the region of the discharge between the electrodes (see section 2.1) only the neutrals loose molecules directly to the reactor walls. Charge transfer collisions lead to the changes in the ion densities in the new equilibrium.

The blue bins show the result for the case if only electrodes are considered is shown. Here, ions are also included (they stream to the electrodes due to the Bohm condition).

5.5. SENSITIVITY OF THE GLOBAL MODEL

For them the same sticking coefficients are used as for the radicals. The surface acts as an ion sink as the ions are assumed to get neutralized approaching the surface. The sticking coefficients computed at an impact energy of 10 eV are taken. Besides the pure fluorine F , F^+ , F_2 and F_2^+ all species densities increase in this case. The decrease of radicals and ions of the same molecule is similar.

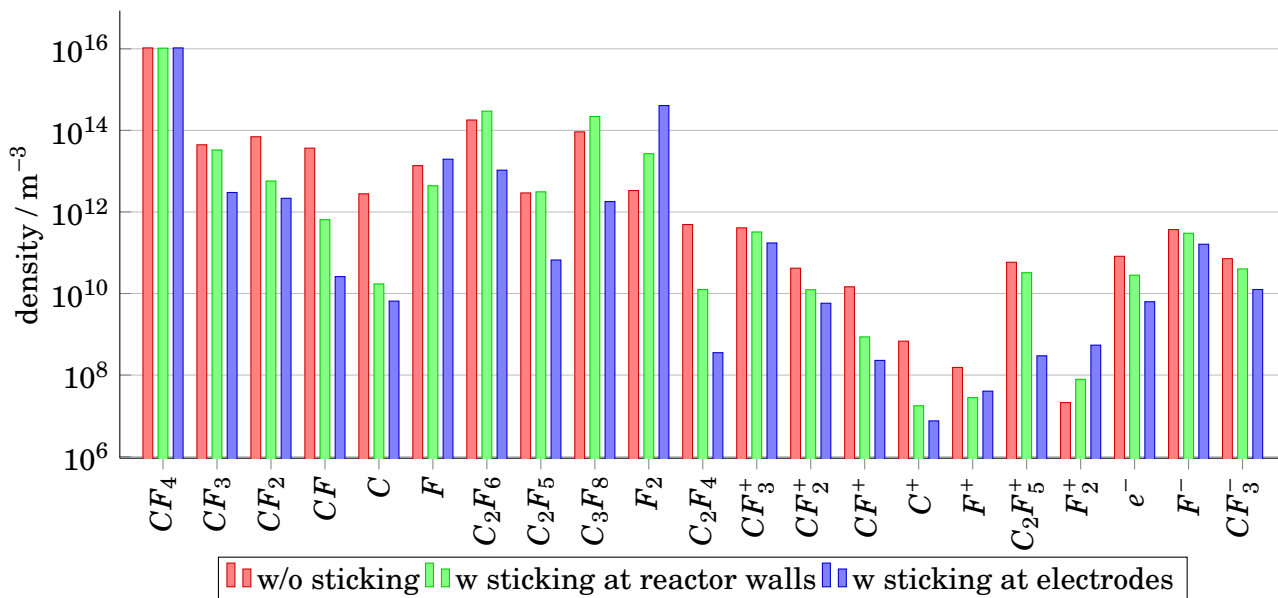


Figure 5.16: Influence of the sticking coefficients in the global model. Overall, a decrease in densities occurs. The decrease is stronger when the sticking coefficients for the electrodes are taken into account (the values computed at 10 eV)

For the low energy case of sticking at the reactor walls a small increase in the densities of large molecules C_2F_6 , C_2F_5 and C_3F_8 appears. The loss of CF and CF_2 is extraordinary high. Therefore, it seems likely that the rise of the density of the large molecules is driven by the fact, that they are assumed to have zero sticking coefficients. That means that they have no loss channel. Improvement of the model would require not only surface *sinks* but also *sources*. However, at the highest investigated energy of 10 eV for the case of electrodes still only sticking but no sputtering occurs, because we are still below sputtering threshold. Therefore, much longer and more runs are needed for this purpose to include the improbable surface reactions at low energies and source through sputtering at higher energies.



6

CONCLUSIONS & OUTLOOK

The major topic of this work was the study of plasma-wall interactions in carbon fluorine plasmas using Molecular Dynamics. Sticking coefficients of various molecules on different films were calculated and their influence in a global 0D model was analyzed, which tries to predict the densities in the bulk region of such plasmas.

The necessary potential is an AIREBO-potential for carbon-hydrogen-fluorine from Jang, which is implemented, tested and validated in the LAMMPS-package. To study the surface reactions CF, CF₃, CF₄, F and CF₂ molecules bombarded surface samples. These surface samples are created by a random allocation procedure combined with different cycles of heating and relaxation. Such, samples with realistic surface and bulk properties are produced. Sticking coefficients are calculated as a function of energy and temperature. They are separated into covalent sticking contributions, due to forming of covalent bonds, and temporal sticking contribution, where the weak bonding is caused by the Lennard-Jones part of the potential. The covalent sticking coefficients in this work are similar to published work on hydrocarbons.

The computed sticking coefficients have a large impact on the global model for carbon fluorine plasmas and change densities significantly. With the currently computed reactions a decrease for most species is reported. The surface temperature influence for the covalent sticking coefficients of CF, as derived from a simplistic analysis model of experimental data by Stepanov can not be reproduced with the current simulation.

The existing work has still several shortcomings mostly due to run-time limits, which can be overcome in possible extensions. The available statistics should be improved to clarify some of the observed trends. The use of the Lennard-Jones potential can not reproduce

CHAPTER 6. CONCLUSIONS & OUTLOOK

the angular dependence of the intermolecular forces resulting in wrong geometries. Also, high energetic photons generated by the plasma can have as much energy as the bonding energy between carbon and fluorine and may cause bond breaking[62–64]. Coupling to collisional-radiative and photon transport models would be necessary.

There are many further applications for the existing work. The extension of the data base for sticking coefficients is straightforward, so that for every species considered in the global model energy dependent sticking coefficients are available. The influence of κ on the sticking can be studied producing more different samples. Analysis of internal energy (e.g. rotational or vibrational) of the incoming molecules gives further insight into the basic physics. Sputter studies could be made with the impinging of high energetic molecules[65]. The results could be compared with studies made with TRIM.SP[66] like done by Reinhold et al. for hydrogen on pure amorphous carbon[67]. A pre-requisite for all these studies is the possibility for a large number of runs. That means access to large scale high-performance computing.

In many applications hydrogen is added into such plasmas[68, 69]. The implemented potential includes already hydrogen and therefore, extension of the work for hydrogen is easily possible. Experiments show a strong influence from this addition. With hydrogen the densities of radicals and the growth rates are considerably higher.



BIBLIOGRAPHY

- [1] DuPont. http://www2.dupont.com/Teflon_Industrial/en_US/tech_info/techinfo_compare.html. June 30, 2012 (cit. on p. 1).
- [2] R.W. Gore. *Process for producing porous products*. US Patent 3,953,566. Apr. 1976 (cit. on p. 1).
- [3] David M. Lemal. "Perspective on Fluorocarbon Chemistry". In: *The Journal of Organic Chemistry* 69.1 (2004). PMID: 14703372, pp. 1–11. DOI: 10.1021/jo0302556 (cit. on p. 1).
- [4] A. R. Ravishankara et al. "Atmospheric Lifetimes of Long-Lived Halogenated Species". In: *Science* 259.5092 (1993), pp. 194–199. DOI: 10.1126/science.259.5092.194 (cit. on p. 1).
- [5] Jakob P. Barz, Christian Oehr, and Achim Lunk. "Analysis and Modeling of Gas-Phase Processes in a CHF₃/Ar Discharge". In: *Plasma Processes and Polymers* 8.5 (2011), pp. 409–423. DOI: 10.1002/ppap.201000095 (cit. on p. 1).
- [6] O.G. Gabriel. "Analyse absoluter Dichten stabiler und transienter Spezies mittels IR-TDLAS in einer fluorkohlenstoffhaltigen Hochfrequenz-Entladung". PhD thesis. EMAU Greifswald, 2005 (cit. on pp. 3, 60).
- [7] S. Stepanov. "Absolute number density and kinetic analysis of CF, CF₂ and C₂F₄ molecules in pulsed CF₄/H₂ rf plasmas". PhD thesis. EMAU Greifswald, 2010 (cit. on pp. 3, 45, 60).
- [8] O Gabriel, S Stepanov, and J Meichsner. "Transient and stable species kinetics in pulsed cc-rf CF₄/H₂ plasmas and their relation to surface processes". In: *Journal of Physics D: Applied Physics* 40.23 (2007), p. 7383. DOI: 10.1088/0022-3727/40/23/020 (cit. on pp. 3, 5, 41).

A Bibliography

- [9] Dongping Liu et al. “Comparison of fluorocarbon film deposition by pulsed/continuous wave and downstream radio frequency plasmas”. In: *Vacuum* 85.2 (2010), pp. 253–262. DOI: 10.1016/j.vacuum.2010.06.005 (cit. on pp. 6, 7).
- [10] Kenneth K.S. Lau and Karen K. Gleason. “Pulsed plasma enhanced and hot filament chemical vapor deposition of fluorocarbon films”. In: *Journal of Fluorine Chemistry* 104.1 (2000), pp. 119–126. DOI: 10.1016/S0022-1139(00)00234-7 (cit. on p. 6).
- [11] Hosun Lee et al. “Spectroscopic ellipsometry and Raman study of fluorinated nanocrystalline carbon thin films”. In: *Journal of Applied Physics* 90.2 (2001), pp. 813–818. DOI: 10.1063/1.1378337 (cit. on p. 6).
- [12] J. P. Booth et al. “CF_x radical production and loss in a CF₄ reactive ion etching plasma: Fluorine rich conditions”. In: *Journal of Applied Physics* 85.6 (1999), pp. 3097–3107. DOI: 10.1063/1.369649 (cit. on pp. 6, 41, 45).
- [13] Hae-suk Jung and Hyung-ho Park. “Structural and electrical properties of co-sputtered fluorinated amorphous carbon film”. In: *Thin Solid Films* 420–421 (2002). Proceedings of the 29th International Conference on Metallurgic Coatings and Thin Films, pp. 248–252. DOI: 10.1016/S0040-6090(02)00802-7 (cit. on pp. 6, 34).
- [14] Yanjun Ma et al. “Structural and electronic properties of low dielectric constant fluorinated amorphous carbon films”. In: *Applied Physics Letters* 72.25 (1998), pp. 3353–3355. DOI: 10.1063/1.121601 (cit. on p. 6).
- [15] Han Jin Ahn et al. “Structural and chemical characterization of fluorinated amorphous carbon films (a-C:F) as a liquid crystal alignment layer”. In: *Diamond and Related Materials* 17.12 (2008), pp. 2019–2024. DOI: 10.1016/j.diamond.2008.06.005 (cit. on p. 6).
- [16] X. Wang et al. “Structural properties of fluorinated amorphous carbon films”. In: *Journal of Applied Physics* 87.1 (2000), pp. 621–623. DOI: 10.1063/1.371910 (cit. on p. 6).
- [17] Hung-Jen Chen et al. “Processing and Characterization of Fluorinated Amorphous Carbon Low-Dielectric-Constant Films”. In: *Journal of The Electrochemical Society* 151.11 (2004), F276–F282. DOI: 10.1149/1.1803835 (cit. on p. 6).
- [18] Z.G. Lu and C.Y. Chung. “Electrochemical characterization of diamond like carbon thin films”. In: *Diamond and Related Materials* 17.11 (2008), pp. 1871–1876. DOI: 10.1016/j.diamond.2008.03.031 (cit. on p. 6).
- [19] S. Tajima and K. Komvopoulos. “Physicochemical Properties and Morphology of Fluorocarbon Films Synthesized on Crosslinked Polyethylene by Capacitively Coupled Octafluorocyclobutane Plasma”. In: *The Journal of Physical Chemistry C* 111.11 (2007), pp. 4358–4367. DOI: 10.1021/jp067521e (cit. on p. 6).
- [20] Carmen I. Butoi et al. “Deposition of Highly Ordered CF₂-Rich Films Using Continuous Wave and Pulsed Hexafluoropropylene Oxide Plasmas”. In: *Chemistry of Materials* 12.7 (2000), pp. 2014–2024. DOI: 10.1021/cm0002416 (cit. on p. 6).
- [21] Peter D. Buzzard, David S. Soong, and Alexis T. Bell. “Plasma polymerization of tetrafluoroethylene in a field-free zone”. In: *Journal of Applied Polymer Science* 27.10 (1982), pp. 3965–3985. DOI: 10.1002/app.1982.070271029 (cit. on p. 6).

-
- [22] Francesca Intranuovo et al. "PECVD of Fluorocarbon Coatings from Hexafluoropropylene Oxide: Glow vs. Afterglow". In: *Chemical Vapor Deposition* 15.4-6 (2009), pp. 95–100. DOI: 10.1002/cvde.200806755 (cit. on p. 6).
- [23] Seung Soon Jang et al. "The Source of Helicity in Perfluorinated N-Alkanes". In: *Macromolecules* 36.14 (2003), pp. 5331–5341. DOI: 10.1021/ma025645t (cit. on pp. 6, 13).
- [24] Hongning Yang et al. "Deposition of highly crosslinked fluorinated amorphous carbon film and structural evolution during thermal annealing". In: *Applied Physics Letters* 73.11 (1998), pp. 1514–1516. DOI: 10.1063/1.122190 (cit. on p. 6).
- [25] Haruo Yokomichi and Atsushi Masuda. "Effect of sputtering with hydrogen dilution on fluorine concentration of low hydrogen content fluorinated amorphous carbon thin films with low dielectric constant". In: *Journal of Applied Physics* 86.5 (1999), pp. 2468–2472. DOI: 10.1063/1.371078 (cit. on p. 6).
- [26] N. Ariel et al. "Deposition temperature effect on thermal stability of fluorinated amorphous carbon films utilized as low-K dielectrics". In: *Materials Science in Semiconductor Processing* 4.4 (2001), pp. 383–391. DOI: 10.1016/S1369-8001(00)00096-2 (cit. on p. 6).
- [27] K. Sasaki et al. "Surface production of CF, CF₂, and C₂ radicals in high-density CF₄/H₂ plasmas". In: *Journal of Applied Physics* 88.10 (2000), pp. 5585–5591. DOI: 10.1063/1.1319974 (cit. on p. 7).
- [28] Peter Fendel, Anne Francis, and Uwe Czarnetzki. "Sources and sinks of CF and CF₂ in a cc-RF CF₄ -plasma under various conditions". In: *Plasma Sources Science and Technology* 14.1 (2005), p. 1. DOI: 10.1088/0963-0252/14/1/001 (cit. on pp. 7, 41).
- [29] Jack D. Dunitz and Robin Taylor. "Organic Fluorine Hardly Ever Accepts Hydrogen Bonds". In: *Chemistry – A European Journal* 3.1 (1997), pp. 89–98. DOI: 10.1002/chem.19970030115 (cit. on p. 7).
- [30] B. J. Alder and T. E. Wainwright. "Phase Transition for a Hard Sphere System". In: *The Journal of Chemical Physics* 27.5 (1957), pp. 1208–1209. DOI: 10.1063/1.1743957 (cit. on p. 9).
- [31] M. Born and R. Oppenheimer. "Zur Quantentheorie der Molekeln". In: *Annalen der Physik* 389.20 (1927), pp. 457–484. DOI: 10.1002/andp.19273892002 (cit. on p. 10).
- [32] J.A. Barker and R.O. Watts. "Structure of water; A Monte Carlo calculation". In: *Chemical Physics Letters* 3.3 (1969), pp. 144–145. DOI: 10.1016/0009-2614(69)80119-3 (cit. on p. 11).
- [33] G. C. Abell. "Empirical chemical pseudopotential theory of molecular and metallic bonding". In: *Phys. Rev. B* 31 (10 May 1985), pp. 6184–6196. DOI: 10.1103/PhysRevB.31.6184 (cit. on p. 11).
- [34] J. Tersoff. "New empirical model for the structural properties of silicon". In: *Phys. Rev. Lett.* 56 (6 Feb. 1986), pp. 632–635. DOI: 10.1103/PhysRevLett.56.632 (cit. on p. 11).
-

A Bibliography

- [35] J. Tersoff. “New empirical approach for the structure and energy of covalent systems”. In: *Phys. Rev. B* 37 (12 Apr. 1988), pp. 6991–7000. DOI: 10.1103/PhysRevB.37.6991 (cit. on pp. 12, 13).
- [36] Donald W. Brenner. “Empirical potential for hydrocarbons for use in simulating the chemical vapor deposition of diamond films”. In: *Phys. Rev. B* 42 (15 Nov. 1990), pp. 9458–9471. DOI: 10.1103/PhysRevB.42.9458 (cit. on p. 13).
- [37] F. Lekien and J. Marsden. “Tricubic interpolation in three dimensions”. In: *International Journal for Numerical Methods in Engineering* 63.3 (2005), pp. 455–471. DOI: 10.1002/nme.1296 (cit. on p. 14).
- [38] D.W. Brenner et al. “A second-generation reactive empirical bond order (REBO) potential energy expression for hydrocarbons”. In: *Journal of Physics: Condensed Matter* 14 (2002), p. 783. DOI: 10.1088/0953-8984/14/4/312 (cit. on pp. 15, 16).
- [39] D. W. Brenner. “The Art and Science of an Analytic Potential”. In: *Computer Simulation of Materials at Atomic Level*. Wiley-VCH Verlag GmbH & Co. KGaA, 2005, pp. 23–40. DOI: 10.1002/3527603107.ch2 (cit. on p. 15).
- [40] Inkook Jang and Susan B. Sinnott. “Molecular Dynamics Simulations of the Chemical Modification of Polystyrene through CxFy+ Beam Deposition”. In: *The Journal of Physical Chemistry B* 108.49 (2004), pp. 18993–19001. DOI: 10.1021/jp049283y (cit. on pp. 15, 16, 18, 22, 29).
- [41] J. Tanaka, C. F. Abrams, and D. B. Graves. “New C–F interatomic potential for molecular dynamics simulation of fluorocarbon film formation”. In: *Journal of Vacuum Science & Technology A: Vacuum, Surfaces, and Films* 18.3 (2000), pp. 938–945. DOI: 10.1116/1.582279 (cit. on p. 15).
- [42] A.C.T. Van Duin et al. “ReaxFF: a reactive force field for hydrocarbons”. In: *The Journal of Physical Chemistry A* 105.41 (2001), pp. 9396–9409. DOI: 10.1021/jp004368u (cit. on p. 15).
- [43] Steven J. Stuart, Alan B. Tutein, and Judith A. Harrison. “A reactive potential for hydrocarbons with intermolecular interactions”. In: *The Journal of Chemical Physics* 112.14 (2000), pp. 6472–6486. DOI: 10.1063/1.481208 (cit. on pp. 18, 20).
- [44] Steve Plimpton. “Fast Parallel Algorithms for Short-Range Molecular Dynamics”. In: *Journal of Computational Physics* 117.1 (1995), pp. 1–19. DOI: 10.1006/jcph.1995.1039 (cit. on pp. 21, 29).
- [45] Axel Kohlmeyer (Temple U). <http://git.icms.temple.edu/lammps-ro.git>. Aug. 13, 2012 (cit. on p. 22).
- [46] C. K. Birdsall and Langdon. “Plasma Physics via Computer Simulation (Series on Plasma Physics)”. In: Taylor & Francis, Jan. 1, 1991. Chap. 2.4, pp. 32, 33 (cit. on p. 23).
- [47] Ralf Schneider, Amit Sharma, and Abha Rai. “Introduction to Molecular Dynamics”. In: *Computational Many-Particle Physics*. Ed. by H. Fehske, R. Schneider, and A. Weiße. Vol. 739. Lecture Notes in Physics. Springer Berlin / Heidelberg, 2008, pp. 3–40. DOI: 10.1007/978-3-540-74686-7_1 (cit. on p. 25).

-
- [48] H. J. C. Berendsen et al. “Molecular dynamics with coupling to an external bath”. In: *The Journal of Chemical Physics* 81.8 (1984), pp. 3684–3690. DOI: 10.1063/1.448118 (cit. on p. 25).
- [49] Glenn J. Martyna et al. “Explicit reversible integrators for extended systems dynamics”. In: *Molecular Physics* 87.5 (1996), pp. 1117–1157. DOI: 10.1080/00268979600100761 (cit. on p. 26).
- [50] A.R. Sharma et al. “Hydrocarbon radicals interaction with amorphous carbon surfaces”. In: *Journal of Nuclear Materials* 363–365 (2007), pp. 1283–1288. DOI: 10.1016/j.jnucmat.2007.01.180 (cit. on pp. 34, 40, 41, 62, 63).
- [51] P. Träskelin, K. Nordlund, and J. Keinonen. “H, He, Ne, Ar-bombardment of amorphous hydrocarbon structures”. In: *Journal of Nuclear Materials* 357.1–3 (2006), pp. 1–8. DOI: 10.1016/j.jnucmat.2005.12.004 (cit. on p. 34).
- [52] E. D. de Rooij, A. W. Kleyn, and W. J. Goedheer. “Sticking of hydrocarbon radicals on different amorphous hydrogenated carbon surfaces: a molecular dynamics study”. In: *Phys. Chem. Chem. Phys.* 12 (42 2010), pp. 14067–14075. DOI: 10.1039/C0CP00637H (cit. on p. 39).
- [53] Oyeon Kum et al. “Molecular dynamics investigation on liquid–liquid phase change in carbon with empirical bond-order potentials”. In: *The Journal of Chemical Physics* 119.12 (2003), pp. 6053–6056. DOI: 10.1063/1.1601216 (cit. on p. 39).
- [54] James N. Glosli and Francis H. Ree. “Liquid-Liquid Phase Transformation in Carbon”. In: *Phys. Rev. Lett.* 82 (23 June 1999), pp. 4659–4662. DOI: 10.1103/PhysRevLett.82.4659 (cit. on p. 39).
- [55] M. Mrovec et al. “Atomistic modeling of hydrocarbon systems using analytic bond-order potentials”. In: *Progress in Materials Science* 52.2–3 (2007). Modelling electrons and atoms for materials science, pp. 230–254. DOI: 10.1016/j.pmatsci.2006.10.012 (cit. on pp. 40, 60).
- [56] P. Träskelin, O. Saresoja, and K. Nordlund. “Molecular dynamics simulations of C₂, C₂H, C₂H₂, C₂H₃, C₂H₄, C₂H₅, and C₂H₆ bombardment of diamond (1 1 1) surfaces”. In: *Journal of Nuclear Materials* 375.2 (2008), pp. 270–274. DOI: 10.1016/j.jnucmat.2007.11.012 (cit. on p. 40).
- [57] D.A. Alman and D.N. Ruzic. “Molecular dynamics calculation of carbon/hydrocarbon reflection coefficients on a hydrogenated graphite surface”. In: *Journal of Nuclear Materials* 313–316 (2003), pp. 182–186. DOI: 10.1016/S0022-3115(02)01428-9 (cit. on p. 41).
- [58] M. Haverlag et al. “Production and destruction of CF_x radicals in radio-frequency fluorocarbon plasmas”. In: *Journal of Vacuum Science & Technology A: Vacuum, Surfaces, and Films* 14.2 (1996), pp. 384–390. DOI: 10.1116/1.580094 (cit. on p. 41).
- [59] Masaru Hori and Toshio Goto. “Measurement techniques of radicals, their gas phase and surface reactions in reactive plasma processing”. In: *Applied Surface Science* 192.1–4 (2002), pp. 135–160. DOI: 10.1016/S0169-4332(02)00024-7 (cit. on pp. 41, 42, 45, 47).
-

A Bibliography

- [60] Da Zhang and Mark J. Kushner. “Surface kinetics and plasma equipment model for Si etching by fluorocarbon plasmas”. In: *Journal of Applied Physics* 87.3 (2000), pp. 1060–1069. DOI: 10.1063/1.371980 (cit. on p. 44).
- [61] S Stepanov and J Meichsner. “Absolute number density and kinetic analysis of the CF radical in pulsed CF₄ + H₂ radio-frequency plasmas”. In: *Plasma Sources Science and Technology* 21.2 (2012), p. 024008. DOI: 10.1088/0963-0252/21/2/024008 (cit. on p. 45).
- [62] J.X. Chen et al. “Photoetching and modification of poly(tetrafluoroethylene-co-hexafluoropropylene) polymer surfaces with vacuum UV radiation”. In: *Polymer Degradation and Stability* 79.3 (2003), pp. 399–404. DOI: 10.1016/S0141-3910(02)00339-7 (cit. on p. 52).
- [63] S. John, S. Langford, and J. Dickinson. “Ablation mechanism of PTFE under 157nm irradiation”. In: *Applied Physics A: Materials Science & Processing* 92 (4 2008), pp. 981–985. DOI: 10.1007/s00339-008-4604-1 (cit. on p. 52).
- [64] Kazuhiko Seki et al. “Electronic structure of poly(tetrafluoroethylene) studied by UPS, VUV absorption, and band calculations”. In: *Physica Scripta* 41.1 (1990), p. 167. DOI: 10.1088/0031-8949/41/1/041 (cit. on p. 52).
- [65] P.R.C. Kent, J. Dadras, and P.S. Krstic. “Improved hydrocarbon potentials for sputtering studies”. In: *Journal of Nuclear Materials* 415.1, Supplement (2011). Proceedings of the 19th International Conference on Plasma-Surface Interactions in Controlled Fusion, S183–S186. DOI: 10.1016/j.jnucmat.2010.08.051 (cit. on p. 52).
- [66] J. P. Biersack and W. Eckstein. “Sputtering studies with the Monte Carlo Program TRIM.SP”. In: *Applied Physics A: Materials Science & Processing* 34 (2 1984), pp. 73–94. DOI: 10.1007/BF00614759 (cit. on p. 52).
- [67] C.O. Reinhold, P.S. Krstic, and S.J. Stuart. “Hydrogen reflection in low-energy collisions with amorphous carbon”. In: *Nuclear Instruments and Methods in Physics Research Section B: Beam Interactions with Materials and Atoms* 267.4 (2009), pp. 691–694. DOI: 10.1016/j.nimb.2008.11.036 (cit. on p. 52).
- [68] E. A. Truesdale and G. Smolinsky. “The effect of added hydrogen on the rf discharge chemistry of CF₄, CF₃H, and C₂F₆”. In: *Journal of Applied Physics* 50.11 (1979), pp. 6594–6599. DOI: 10.1063/1.325908 (cit. on p. 52).
- [69] R. Knizikevičius. “Real dimensional simulation of SiO₂ etching in CF₄+H₂ plasma”. In: *Vacuum* 65.1 (2002), pp. 101–108. DOI: 10.1016/S0042-207X(01)00413-4 (cit. on p. 52).
- [70] K. Tichmann et al. “Determination of the sticking probability of hydrocarbons on an amorphous hydrocarbon surface”. In: *Physica Scripta* 2009 (2009), p. 014015. DOI: 10.1088/0031-8949/2009/T138/014015 (cit. on pp. 62, 63).
- [71] K. Nordlund, J. Keinonen, and T. Mattila. “Formation of Ion Irradiation Induced Small-Scale Defects on Graphite Surfaces”. In: *Phys. Rev. Lett.* 77 (4 July 1996), pp. 699–702. DOI: 10.1103/PhysRevLett.77.699 (cit. on p. 62).



B

APPENDIX

B.1 Basic Equations

B.1.1 Thermodynamic properties

The total kinetic energy and therefore the temperature is calculated from the kinetic energy of each particle. In the calculation of temperature the number of dimensions are neglected in the degrees of freedom d , as the orientation of the coordinate system can be chosen arbitrarily.

$$\mathcal{E}_{kin} = \sum_i \frac{m_i \cdot v_i^2}{2} \quad (\text{B.1.1})$$

$$= \frac{d}{2} \cdot (N - 1) \cdot k_B \cdot T \quad (\text{B.1.2})$$

The pressure is calculated with the virial term $\sum_i^N \sum_{j(>i)} r_{ij} \cdot \mathbf{F}_{ij}$ ($\mathbf{F}_{ij} = - \left. \frac{d\phi_{ij}}{dr} \right|_{ij}$ - force between particle i and j)

$$\mathcal{P} = \frac{N \cdot k_b \cdot T}{V} + \frac{\sum_i^N \sum_{j(>i)} r_{ij} \cdot \mathbf{F}_{ij}}{d \cdot V}. \quad (\text{B.1.3})$$

B.1.2 Unbiased estimators for statistical analysis

The following statistical estimators are used to calculate values during the computation with a varying number of runs ω_i per sample i :

- weighted arithmetic mean

$$\bar{x} = \frac{\sum_{i=1}^N \omega_i x_i}{\sum_{i=1}^N \omega_i} \quad (\text{B.1.4})$$

- weighted variance equal to squared standard derivation

$$\sigma^2 = \frac{\sum_{i=1}^N \omega_i x_i^2 \cdot \sum_{i=1}^N \omega_i - (\sum_{i=1}^N \omega_i x_i)^2}{(\sum_{i=1}^N \omega_i)^2} \quad (\text{B.1.5})$$

- weighted confidence interval of the arithmetic mean

$$\bar{\sigma}^2 = \frac{\left[\sum_{i=1}^N \omega_i x_i^2 \cdot \sum_{i=1}^N \omega_i - (\sum_{i=1}^N \omega_i x_i)^2 \right] \cdot \sum_{i=1}^N \omega_i^2}{\left[(\sum_{i=1}^N \omega_i)^2 - \sum_{i=1}^N \omega_i^2 \right] \cdot (\sum_{i=1}^N \omega_i)^2} \quad (\text{B.1.6})$$

B.1.3 Derivation of a new switching term

The system of equations follows from the constraints for the values and derivatives. With $t(r_{ij}) = \frac{r_{ij} - r_{ij}^{\min}}{r_{ij}^{\max} - r_{ij}^{\min}}$ one gets for the calculation of the switching function $f(x)$ the system of equations with $t(r_{ij}^{\min} = 0)$ and $t(r_{ij}^{\max} = 1)$:

$$\begin{aligned} f(0) &= 1 & f(0.5) &= 0.5 & f(1) &= 0 \\ f'(0) &= 0 & & & f'(1) &= 0 \\ f''(0) &= 0 & & & f''(1) &= 0 \end{aligned} \quad (\text{B.1.7})$$

For the Hermite interpolation the solution is written with Horner's method

$$p(x) = 1 + x^3(x(15 - 6x) - 10) \quad (\text{B.1.8})$$

The original and the new switching functions are compared in Figure B.1. The occurring bumps in the derivative lead to a modification of the force acting in the cut-off region. As the force is strongly increased in comparison to the case without cut-off function wrong stress tensors may be computed operating in this regime. For such cases, the switch function is multiplied with the force[55].

B.1.4 Plasma reactions

Example plasma reactions from [6] and [7] considered in the 0D-model.

dissociative ionization



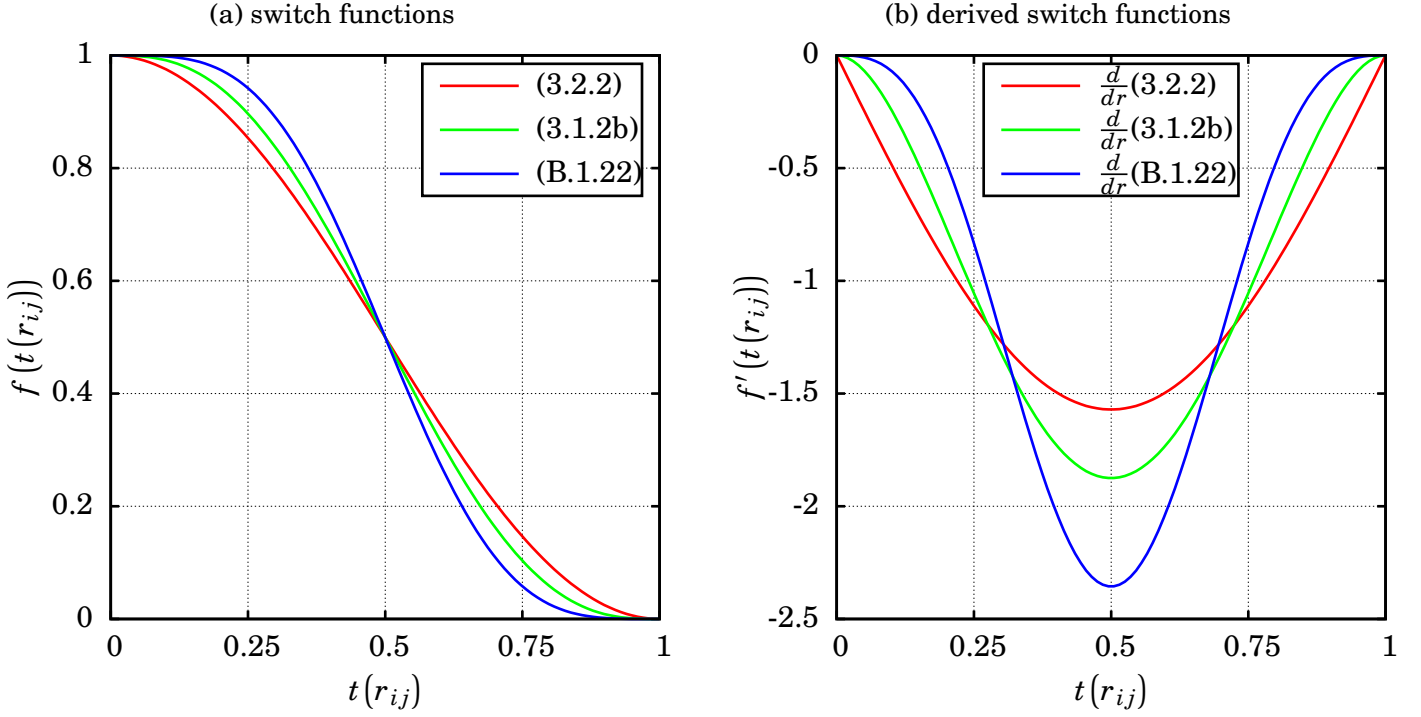


Figure B.1: In B.1a the evaluated switches are presented. In B.1b their derivations.

e^- dissociation



e^- dissociation



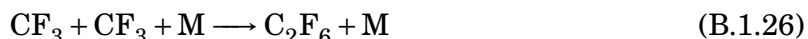
e^- dissociation with ionization



e^- dissociative attachment

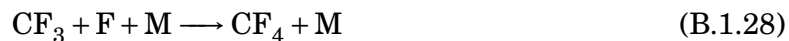


Gas-phase or surface three body reactions

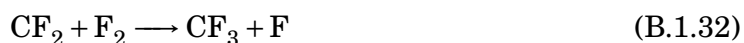


Main recombination reactions of radicals:

three-body radical sink



with fluorine molecules



B.1.5 Relation between impact energy and impact angle

The sticking coefficients $\beta(\alpha)$ for different impact angles at a single impact energy can be approximated from the sticking coefficients $\beta(E)$ for impacts normal to the surface. This assumption holds true as long as no sputtering of the surface occurs.

Assuming that only the energy of the velocity perpendicular to the surface is important for the sticking coefficient β , one gets with the angle α between the surface normal and the center of mass velocity of the incoming molecule

$$E_{eff.}(\alpha) = E_{\perp} = \frac{m \cdot v_{\perp}^2}{2} = \frac{m \cdot (v \cdot \cos \alpha)^2}{2} = E \cdot \cos^2 \alpha. \quad (\text{B.1.34})$$

This ansatz is inserted in the fitting formulas for CH_3 in Tichmann[70] to convert $\beta(\mathcal{E})$ into $\beta(\alpha)$ (see Fig. B.2). As the fitting formula is only valid for energy larger than 5 eV an additional expression is necessary to describe angles close to 90°. Fortunately, Sharma[50] has made similar calculations with the same code[71] and for the same hydrogen and carbon fraction $\kappa = 0.66$. Since the sticking coefficient at 5 eV differs between these papers by about 40%, only the linear fit from the logarithmic scaled plot is taken from Sharma and the fitting equation is expanded to

$$f(x) = a \cdot \log x + b \quad (\text{B.1.35a})$$

$$= 0.0993 \cdot \log x + 0.358. \quad (\text{B.1.35b})$$

Because the normal impact with 5 eV is equivalent to an impact with 50 eV at an angle of 71.6°, the error in Fig. B.2a for smaller angles may be introduced by sticking at surfaces bumps. Nonetheless, the maximum difference in both figures is around ≈ 0.1 , which is smaller than the difference between [70] and [50] at 5 eV with ≈ 0.4 . Therefore, for small energies without sputtering relation (B.1.34) should give an approximation within the statistical errors of the simulation.

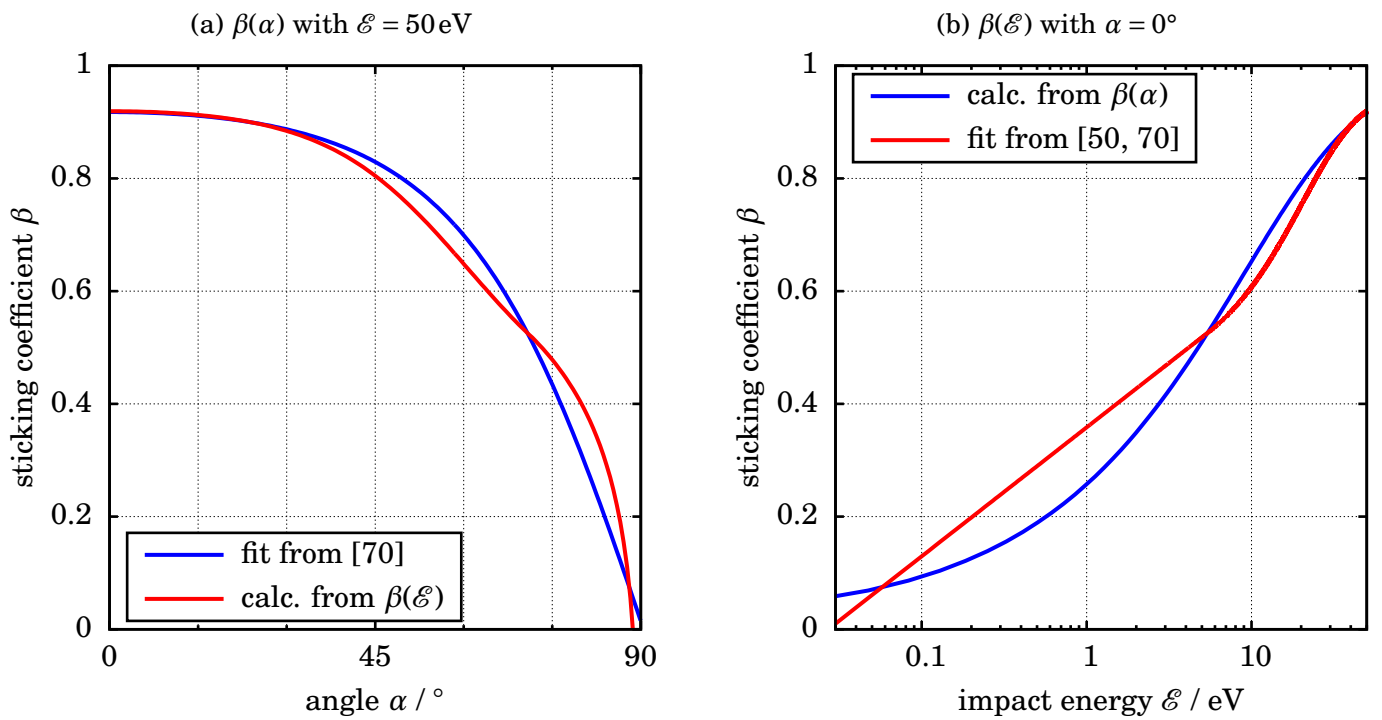


Figure B.2: Sticking coefficient β in dependence of molecule impact energy \mathcal{E} and impact angle α normal to the surface at $\mathcal{E} = 50 \text{ eV}$ for CH_3 . Via the relation (B.1.34) the fit for $\beta(\mathcal{E})$ is plotted as $\beta(\alpha)$ and the other way round.

B.2 Coefficients Tables

	C-C	C-F	F-F	C-H	H-H	H-F
A / eV	10953.54416216992	909.2022	16451.97	149.940987228812	31.6731	887.0513
$B_{ij}^{(1)}$ / eV	12388.79197798375	219.7799	146.8149	32.35518665873256	28.2297	571.1737
$B_{ij}^{(2)}$ / eV	17.56740646508968					
$B_{ij}^{(3)}$ / eV	30.71493208065162					
Q / Å	0.3134602960832605			0.3407757282257080	0.370	
α / Å ⁻¹	4.746539060659529	3.7128	6.8149	4.102549828548784	3.536	3.7789
$\beta_{ij}^{(1)}$ / Å ⁻¹	4.720452312717397	2.1763	2.8568	1.434458059249837	1.708	3.0920
$\beta_{ij}^{(2)}$ / Å ⁻¹	1.433213249951261					
$\beta_{ij}^{(3)}$ / Å ⁻¹	1.382691250599169					
ρ_{ij} / Å		1.09	0.7415887	1.2718	1.4119	0.9378
r_{ij}^{\min} / Å	1.7	1.7	1.7	1.3	1.1	1.3
r_{ij}^{\max} / Å	2.0	2.0	2.0	1.8	1.7	1.8

Table B.1: Values used for the covalent part of the AIREBO-potential.

	C-C	C-F	F-F	C-H	H-H	H-F
ϵ_{ij} / eV	0.0028437324	0.004870596	0.005376993	0.0020639767	0.0014994226	0.0028394338
σ_{ij} / Å	3.4	3.08	2.81	3.025	2.65	2.73
$r_{ij}^{\text{LJ min}}$ / Å	3.4	3.08	2.81	3.025	2.65	2.73
$r_{ij}^{\text{LJ max}}$ / Å	3.816370964	3.395447696	2.974524428	3.457183108	3.154118355	3.064321392
$b_{ij}^{\text{LJ min}}$	0.77	0.75	0.32	0.75	0.32	0.32
$b_{ij}^{\text{LJ max}}$	0.81	0.9	0.42	0.9	0.42	0.42

Table B.2: Values used for the Lennard-jones-potential in the AIREBO-potential.

molecule	surface number			
	1	2	7	8
F		62(5) %		80(5) %
C ₂			96(3) %	
CF ₃	27(9) %			13(7) %
C ₂ F ₂			33(8) %	

Table B.3: Loss probability for additional surface molecules during the computation of the sticking coefficient for atomic fluorine.

B.3 Additional Figures

B.3.1 Atomization energy validation

To test the potential implementation atomization energies for various configurations are shown in Figure B.3 (see section 5.1). For hydrocarbons the agreement is excellent, but when fluorine is bonded at carbon atoms with four bonds the deviation gets large.

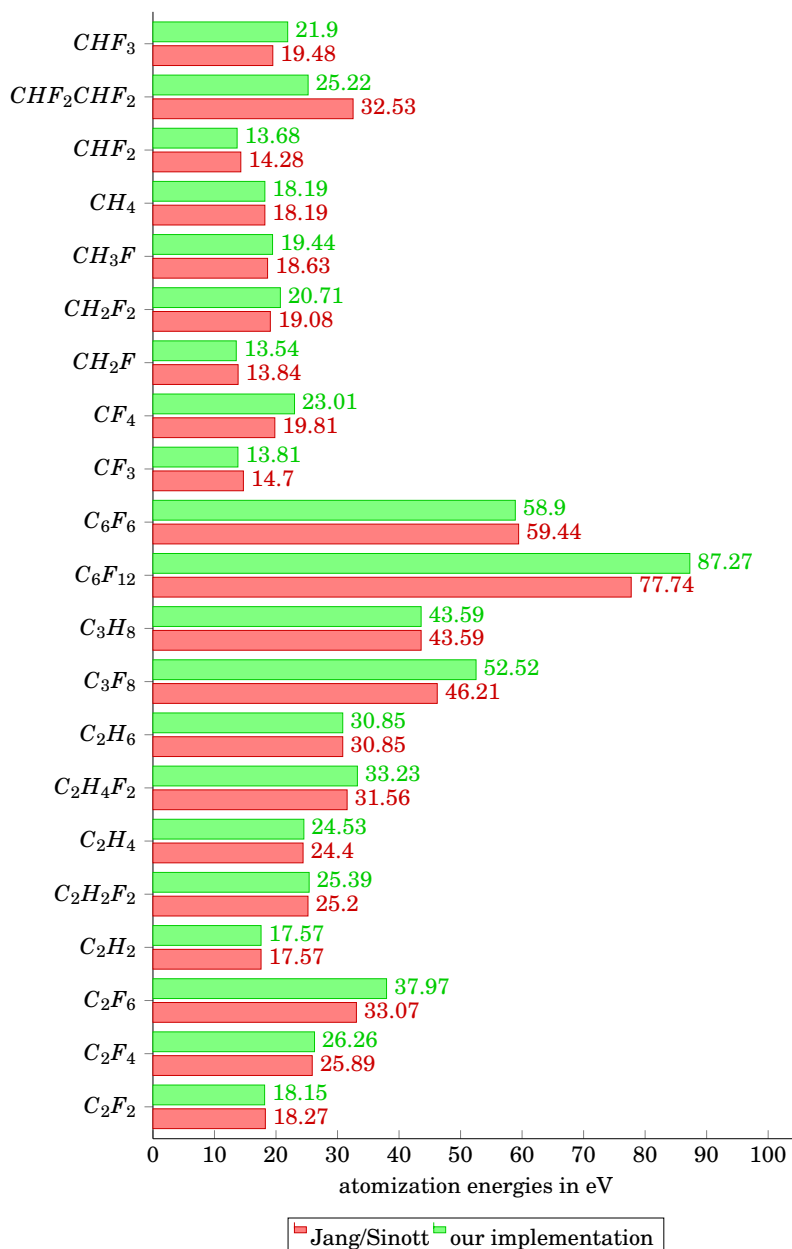


Figure B.3: Atomization energies for selected species.

B.3.2 Frequency analysis of the barostat

The Discrete Fourier Analysis of the volume oscillation driven by the barostat is shown in Figure B.4(see section 5.3.2). Low frequencies are stronger populated. In the auto-correlation function no periodic structure appears (see Figure B.5). The process looks like a “moving average process”, but no further analysis was done.

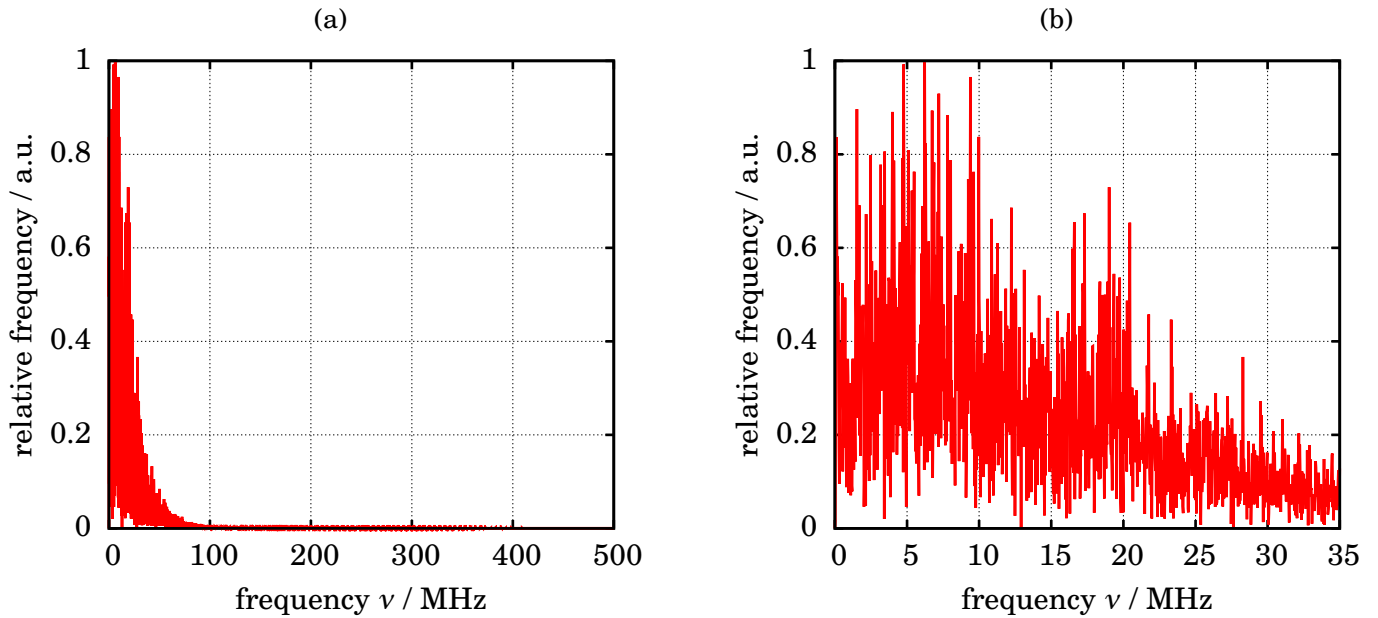


Figure B.4: Discrete Fourier Analysis during the failed barostat relaxation.

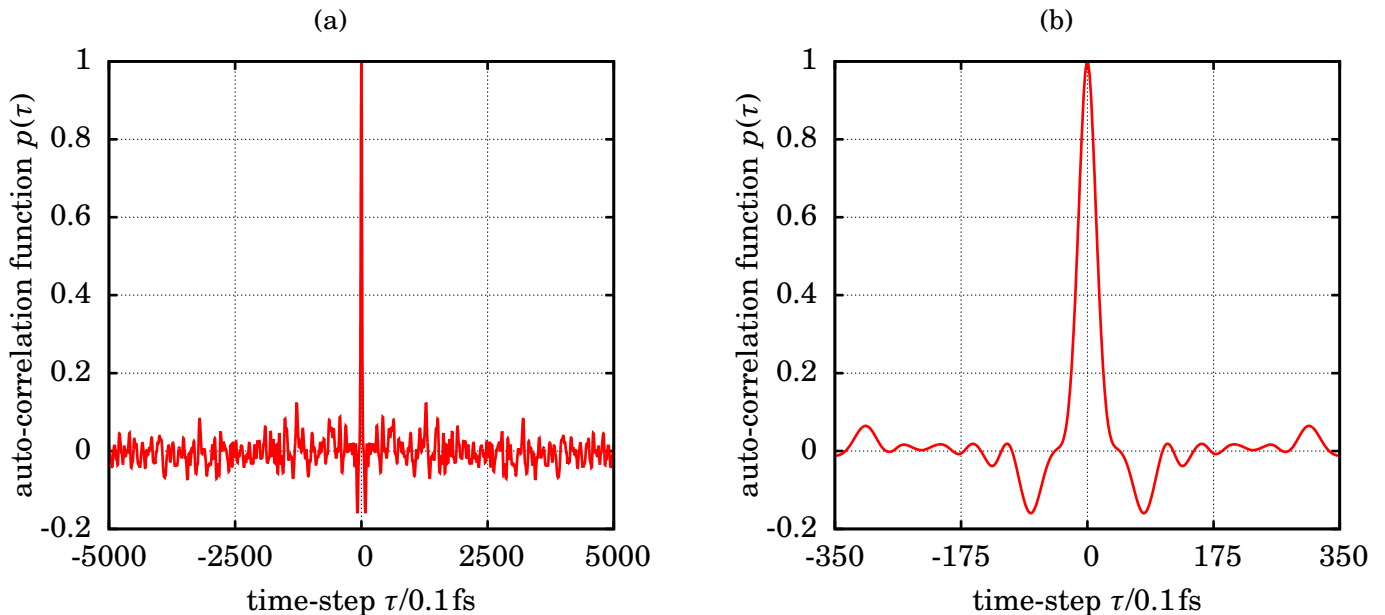


Figure B.5: Auto-correlation function of the oscillating temperature during the failed barostat run Fig. 5.7.

B.3.3 Additional sample

In Figure B.6 a generated surface with $\kappa = 1.2$ is shown. This surface was produced through random allocation of fluorine and carbons and is an intermediate state between surface 1 and 2 in Figure 5.8. The large red molecule consists of over one third of all carbon atoms and is the carrying skeleton of the surface. Surface molecules like the orange one may be detached through fast impinging molecules.

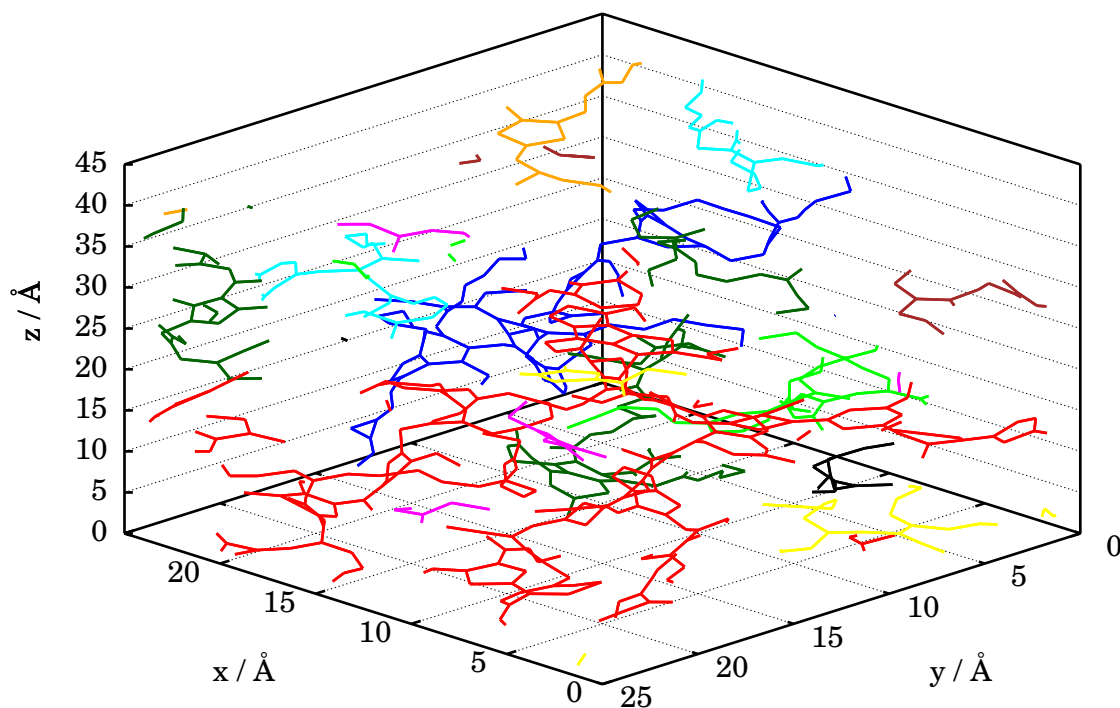


Figure B.6: Surface with $\kappa = 1.2$ generated by random allocation of atomic fluorine and carbon.



ACKNOWLEDGMENT

At the end I like to thank all the people, whose support me. Gunnar and Ralf I like to thank for all the insights and instructions. Tim and Konstantin for the general coding advises. Lars, Julia and Abra for proof reading. Sascha, Henry and Matthias for the technical support, namely the clusters. A thanks to the open-source community for developing LAMMPS, GNUEmacs, Gnuplot, GNUOctave, Mercurial, Mplayer & vlc, LaTeX, Ispell, Wikipedia, Linux Mint and Arch Linux. And for various kinds of support I would like to give a special thanks to my parents, Katrin and Volker.